Age Gradients in the Stellar Populations of Massive Star Forming Regions Based on a New Stellar Chronometer

Konstantin V. Getman[1], Eric D. Feigelson[1,2], Michael A. Kuhn[1], Patrick S. Broos[1], Leisa K. Townsley[1], Tim Naylor[3], Matthew S. Povich[4], Kevin L. Luhman[1,2], Gordon P. Garmire[5]

Received _____; accepted _____

Accepted for publication in ApJ, 02/12/14

[1]Department of Astronomy & Astrophysics, 525 Davey Laboratory, Pennsylvania State University, University Park, PA 16802, USA

[2]Center for Exoplanets and Habitable Worlds, Pennsylvania State University, University Park, PA 16802, USA

[3]School of Physics and Astronomy, University of Exeter, Stocker Road, Exeter, EX4 4QL, UK

[4]Department of Physics and Astronomy, California State Polytechnic University, 3801 West Temple Ave, Pomona, CA 91768, USA

[5]Huntingdon Institute for X-ray Astronomy, LLC, 10677 Franks Road, Huntingdon, PA 16652, USA

ABSTRACT

A major impediment to understanding star formation in massive star forming regions (MSFRs) is the absence of a reliable stellar chronometer to unravel their complex star formation histories. We present a new estimation of stellar ages using a new method that employs near-infrared (NIR) and X-ray photometry, Age_{JX}. Stellar masses are derived from X-ray luminosities using the $L_X - M$ relation from the Taurus cloud. J-band luminosities are compared to mass-dependent pre-main-sequence evolutionary models to estimate ages. Age_{JX} is sensitive to a wide range of evolutionary stages, from disk-bearing stars embedded in a cloud to widely dispersed older pre-main sequence stars. The MYStIX (Massive Young Star-Forming Complex Study in Infrared and X-ray) project characterizes 20 OB-dominated MSFRs using X-ray, mid-infrared, and NIR catalogs. The Age_{JX} method has been applied to 5525 out of 31,784 MYStIX Probable Complex Members. We provide a homogeneous set of median ages for over a hundred subclusters in 15 MSFRs; median subcluster ages range between 0.5 Myr and 5 Myr. The important science result is the discovery of age gradients across MYStIX regions. The wide MSFR age distribution appears as spatially segregated structures with different ages. The Age_{JX} ages are youngest in obscured locations in molecular clouds, intermediate in revealed stellar clusters, and oldest in distributed populations. The NIR color index $J - H$, a surrogate measure of extinction, can serve as an approximate age predictor for young embedded clusters.

Subject headings: infrared: stars; stars: early-type; open clusters and associations: general; stars: formation; stars:pre-main sequence; X-rays: stars

1. Introduction

Infrared (IR) and millimeter astronomy, together with astrophysical theory, have made great progress in understanding the formation of single stars in small molecular cloud cores on ≤ 0.1 pc scales. However, most stars do not form in such simple environments, arising rather in turbulent giant molecular clouds where different modes of star formation are seen: rich OB-dominated stellar clusters, smaller clusters in dense IR Dark Clouds and filaments, and stellar groups on the peripheries of expanding H II regions. It is not clearly known how cloud cores and filaments form, whether clusters form during a single free-fall time or over millions of years, or whether triggering by H II regions or supernova remnants play minor or major roles. Combined infrared and X-ray surveys, such as the *Chandra Carina Complex Project* (CCCP; Townsley et al. 2011), have the advantage of locating both recently formed disk-bearing (proto)stars and older pre-main sequence (PMS) stars. These studies reveal spatially distinct clusters that appear to have different ages, and often a population of older widely distributed stars dispersed from earlier generations of star formation. Our group is now engaged in the Massive Young Star-Forming Complex Study in Infrared and X-ray (MYStIX; Feigelson et al. 2013) that examines 20 star forming complexes. MYStIX fields include a range of small and large cloud structures producing sparse and rich stellar clusters.

A major impediment to understanding star formation in massive star forming regions (MSFRs) has been the absence of a reliable stellar chronometer so that the star formation history in a region can be reconstructed. While embedded protostars with Class 0 and Class I infrared spectral energy distributions (IR SEDs) clearly represent the most recent episodes of star formation activity, the sequence of past activity is difficult to unravel from IR SEDs alone because dusty protoplanetary disks have a wide range of longevities. Approximately 10% of stars lose their disks in ≤ 0.5 Myr, 10% retain their disks for ≥ 6 Myr, and

the remaining 80% have disk longevities smoothly distributed between 0.5 and 6 Myr (Hernández et al. 2008; Mamajek 2009). The disk fraction commonly used to estimate the age of a young stellar sample (Haisch et al. 2001, and citations thereof), roughly the ratio #(Class I + Class II)/#(Class I + Class II + Class III), therefore can only give a crude measure of stellar ages. Other stellar properties once proposed as chronometers, such as the depletion of photospheric lithium or the evolution of stellar rotation, do not show simple scalings with stellar age during the PMS phase (Piau & Turck-Chièze 2002; Eggenberger et al. 2012; Bouvier 2013).

The best hope for an accurate stellar age estimator during the PMS evolutionary phase has been location on the Hertzsprung-Russell diagram (HRD) or photometric color-magnitude diagram (CMD), where stars of a fixed mass are predicted to progress along distinct tracks defined by convective interior models. Unfortunately, many problems are now recognized to affect a star's location in HRDs: photometric variability from accretion and magnetic activity, different accretional histories, binarity, extinction uncertainty, veiling from accretion, scattering and absorption by disks, stellar interiors model uncertainty, and distance uncertainty (e.g., Baraffe et al. 2009; Naylor 2009; Soderblom 2010; Jeffries et al. 2011; Jeffries 2012). These issues have recently been reviewed by Preibisch (2012) who emphasizes that 'severe misinterpretations, gross overestimates of the age spread, and ill-based conclusions about the star formation history' can result from insufficient treatment of these effects. Preibisch also emphasizes the importance of disentangling the distinct subgroups that are often present in a star forming region in order to establish the 'temporal sequence of several discrete star formation episodes'.

In §§2 and 3, we describe a new PMS stellar age estimator, Age_{JX}, that depends on near-IR stellar photospheric emission and on hard X-ray luminosity which arises mostly from enhanced magnetic flaring of PMS stars. Near-IR and X-ray photometric measurements

are provided in surveys such as CCCP and MYStIX where they are used in the selection of MSFR members. Age_{JX} is applied only to carefully chosen subsamples of members with appropriate near-IR and X-ray data, and is based on an empirical X-ray/mass relation calibrated to well-studied Taurus PMS stars (Telleschi et al. 2007) and to theoretical evolutionary tracks calculated by Siess et al. (2000). This age estimate mitigates some (although not all) of the above problems encountered in HRD- and CMD-based chronometry (§5). Individual star Age_{JX} values for the MYStIX MSFRs range from < 1 to ~ 5 Myr (Table 1).

As with other methods, we find a range of PMS Age_{JX} values in large-scale MSFRs that could be considered to be a general wide spread in ages (§3.2-4). But, in accord with the advice of Preibisch (2012), we recompute ages averaged over spatially distinct subclusters (§4) that were recently obtained by Kuhn et al. (2014) for MYStIX MSFRs. In that study, a statistical 'finite mixture model' of isothermal ellipsoids was fit to the sky distribution of probable cloud members using maximum likelihood techniques. Each star can then be assigned as a member of a specific subcluster or as a member of a distributed unclustered population.

The result of computing Age_{JX} averaged over these subclusters is often remarkable: the full MSFR age distribution spanning several million years now appears as spatially segregated structures with narrowly constrained ages. Furthermore, we often see that the subclusters form spatial-absorption gradients consistent with astronomically reasonable patterns of star formation histories, with older lightly absorbed structures on one side, younger heavily absorbed structures on the other side, and intermediate-age structures in the middle (§7). Widely distributed populations are nearly always older. The progression of star formation within a MSFR can be traced, and patterns of star formation histories can be compared between MSFRs. We provide a homogeneous set of averaged Age_{JX} for a

hundred subclusters and regions of interest in MYStIX MSFRs (Table 2).

2. The Age_{JX} Method

2.1. Concept

The method developed here has three steps.

1. The stellar mass (M) is derived from the intrinsic X-ray luminosity measurement (L_X) of a star using the well-established empirical $L_X - M$ relationship for PMS stars of Telleschi et al. (2007) (§3.1).

2. The sample is truncated to include only low-mass stars and the absolute J-band magnitude (M_J) is derived by correcting the apparent J magnitude for a photometrically estimated absorption A_J and distance. Notice that, unlike optical magnitudes (or IR magnitudes at longer wavelengths), J is less prone to the effects of absorption, accretion, and diffuse nebular background (or disks and nebular background) (§5). J is more prone to the effects of absorption than H and K near-infrared magnitudes, but is less affected by thermal disk emission.

3. We estimate stellar ages Age_{JX} using obtained mass estimate M and the absolute J-band magnitude M_J by comparison to the PMS isochrones of Siess et al. (2000). This $M_J - M$ diagram is a surrogate for the traditional HRD (Figure 1).

The observational inputs to the calculation are: the distance to the MSFR[1], the absorption-corrected X-ray luminosity in the $(0.5 - 8)$ keV energy band, and the apparent JHK_s

[1]To calculate both L_X and M_J we use distances to each MSFR adopted for the MYStIX project (Table 1 of Feigelson et al. 2013).

magnitudes as well as the $L_X - M$ and interstellar reddening calibration relations and theoretical evolutionary tracks.

2.2. Sample selection

The 31,784 MYStIX Probable Complex Members (MPCMs) constitute the initial stellar sample for this study (Broos et al. 2013). The MPCM sample is extracted from source catalogs constructed by special analysis of data from the *Chandra X-ray Observatory*, *Spitzer Space Telescope*, United Kingdom Infra-Red Telescope, and 2MASS telescopes. The MPCMs are a union of statistically classified X-ray selected stars, photometric infrared excess stars, and published OB stars. The multistage construction of the MPCM sample is described by Feigelson et al. (2013) and its accompanying papers. Kuhn et al. (2013a) and Townsley et al. (2013) present X-ray sources and properties, King et al. (2013) present the near-IR sources and properties, Kuhn et al. (2013b) present the mid-IR sources and properties, Naylor et al. (2013) describe the X-ray/infrared source matching procedure, Povich et al. (2013) identify infrared-excess stars, and Broos et al. (2013) statistically derive the integrated sample of MPCMs in the 20 MYStIX MSFRs.

Intrinsic stellar X-ray luminosities L_X (in the $0.5 - 8$ keV band) are determined in a uniform way using the non-parametric method $XPHOT$ (Getman et al. 2010). $XPHOT$ is applicable to X-ray sources with greater than several net counts, and allows an approximate recovery of the soft ($\lesssim 1$ keV) X-ray plasma component, which is often missed in the X-ray data of weak and/or highly absorbed sources when using traditional methods of parametric model fitting, such as XSPEC. We therefore distill, from the full MPCM catalog, sources with XPHOT L_X estimates.

Individual stellar age estimates Age_{JX} are restricted to 5525 MPCM members. First,

the full MPCM sample was restricted to stars with sufficient X-ray counts to have an $XPHOT$ estimate of L_X. All MYStIX Infrared Excess (MIRES; Povich et al. 2013) sources without X-ray counterparts, and very faint X-ray sources, are omitted. Second, three MYStIX regions (W 3, W 4, and NGC 3576), which were not subject to spatial clustering analysis by Kuhn et al. (2014), and two MYStIX regions (RCW 38 and Trifid Nebula) with poor Age_{JX} sampling are ignored from our detailed age analysis. Third, the X-ray source sample is truncated to retain sources with reliable NIR photometry, retaining sources with uncertainties on individual JHK_s measurements of < 0.1 mag or uncertainties on $J - H$ and $H - K_s$ colors of < 0.1 mag. This permits reasonably accurate absorption correction.

Fourth, the sample is culled of objects with large K_s-excesses for which there is no clear NIR dereddening procedures. Objects with $H - K_s$ colors redder than those of the well studied disk-bearing stars in the Taurus star forming region are removed from the sample (Figure 2). Many of these objects with extreme K-excess emission are likely protostars (Lada et al. 2000). Future MYStIX papers will focus on properties of these objects. Finally, we apply two cuts to the sample to restrict consideration to lower-mass stars that follow convective Hayashi tracks in the HRD. First, stars with $L_X > 3 \times 10^{30}$ erg s^{-1} are removed. From the $L_X - M$ calibration curve of Telleschi et al. (2007), this deletes stars with $M \gtrsim 1.2$ M$_\odot$. Second, stars with $J - H > 0.5$ mag are removed; this excludes lightly absorbed hotter early-type stars.

It is important to note that for the stars in the final MYStIX Age_{JX} sample, the typical number of X-ray net counts per source is ~ 20 counts and the typical Poisson noise and modeling uncertinties on X-ray luminosity inferred by the XPHOT method are $\sigma/L_X \sim 40 - 50\%$ each.

Thus from the original 31,784 MPCM stars, we are left with a subsample of 5525 well-characterized relatively X-ray-bright low-mass stars for Age_{JX} determination.

2.3. Dereddening

The extinctions in the J-band (A_J) are derived from dereddening to the intrinsic color locus of the Taurus low-mass stars in the $J-H$ vs. $H-K_s$ color-color diagram (Figure 2). The Taurus locus is produced using the data of Luhman et al. (2010) (and K. Luhman, private communication); the reddening laws $A_J/A_{K_s} = 2.5$ and $A_H/A_{K_s} = 1.55$ are used (Indebetouw et al. 2005). The absolute magnitudes M_J are then determined from J, A_J, and the MYStIX region distance estimates compiled by Feigelson et al. (2013). Notice that the XPHOT L_X estimates are totally independent of NIR reddening; L_X's were corrected for absorption using X-ray median energies as surrogates for X-ray absorption column densities, as described by Getman et al. (2010).

2.4. Mass and age estimation

Stellar mass estimates are derived from the L_X values using the clear (but poorly understood; §3.1) regression relationship $\log(L_X) = 1.69 \times \log(M/M_\odot) + 30.33$ found for PMS stars in the Taurus region (Telleschi et al. 2007). The minor effect of the weak temporal evolution of X-ray luminosity in PMS stars (Preibisch & Feigelson 2005), if real, is ignored in our analysis (§3.1).

Age_{JX} estimates are then produced by minimizing χ^2 between the observed absorption-corrected J-band magnitudes and X-ray-based mass estimates (M_J, σ_{M_J}, M, σ_M) and the grid of evolutionary tracks associated with the PMS stellar interior models of Siess et al. (2000). The age step in this grid is 0.1 Myr. Since smaller M_J separations among older isochrones on the $M_J - M$ diagram could result in unrealistically high individual age estimates, the evolutionary models used here stop at 5 Myr. The resulting Age_{JX} estimates for 5525 MYStIX stars are given in Table 1 along with the MYStIX designation,

sky coordinates, NIR photometry, absorption-corrected X-ray luminosity, and cluster membership from Kuhn et al. (2014).

3. Understanding the Age_{JX} Method

Before presenting the results from the Age_{JX} method on the ages of the MYStIX regions and subclusters (§4), in the current section, we discuss various aspects of the Age_{JX} estimates of PMS ages: the underlying relationships between stellar properties, sources of uncertainty and scatter, and comparison with other methods.

3.1. Relationship between X-ray Luminosity and Mass

The Age_{JX} method relies on an assumption of a universal $L_X - M$ relationship for $\lesssim 5$ Myr old PMS stars. The relationship was originally found in *ROSAT* studies of nearby star forming regions (Feigelson et al. 1993), and has been described in major studies of the Taurus (XEST; Telleschi et al. 2007) and Orion Nebula Cluster (COUP; Preibisch et al. 2005) populations. The correlation in Taurus stars is tighter than in Orion stars, probably due to their more reliable stellar mass estimates. $L_X - M$ distributions similar to that seen in Taurus and the ONC are seen in other regions; for instance, in the $1-3$ Myr old NGC 2264 region (Flaccomio et al. 2006), the $2-3$ Myr old Cep OB3b region (Getman et al. 2006, 2009), the $\lesssim 1$ Myr old W 40 region (Kuhn et al. 2010), and the $2-3$ Myr old IC 348 region (Stelzer et al. 2012). The sources of scatter in the $L_X - M$ relationship will be statistical noise, X-ray variability from magnetic activity, binarity, intrinsic imperfection of the relationship, modeling uncertainties on L_X and mass, and suppression of time-integrated X-ray emission in accreting versus non-accreting stars.

While both accreting 'classical' T Tauri stars and non-accreting 'weak-line' T Tauri

stars have broad X-ray luminosity functions ranging from $\log L_X \simeq 28 - 31$ erg s^{-1}, it was found with *ROSAT* (Neuhaeuser et al. 1995) that the X-ray luminosity function of accreting stars is somewhat lower than that of non-accreting stars. This is seen despite the frequent presence of a soft X-ray component associated with the accretion spot on the stellar surface (Güdel & Telleschi 2007). However, the effect could be mass dependent: for the PMS population in the nearby Taurus region, Telleschi et al. (2007) report that accreting stars are less X-ray active than non-accreting stars for a wide range of masses (> 0.3 M$_\odot$); meanwhile, for the richer PMS populations in the more distant Orion Nebula Cluster and IC 348 region, Preibisch et al. (2005) and Stelzer et al. (2012) report no differences in X-ray activity between accreting and non-accreting stars in the mass range $\sim 0.5 - 1.2$ M$_\odot$. The latter is a typical mass range for the MYStIX-Age_{JX} stars (Figure 1).

On the other hand, PMS stars lie coincident with the activity-saturation locus of main-sequence (MS) stars on the L_X/L_{bol}-Rossby (or L_X/L_{bol}-Rotation) diagram; albeit, the scatter in L_X/L_{bol} is large. Examples of the activity-Rossby relationship for the PMS stars in ONC, Taurus, NGC 2264, and IC 348 can be found in Preibisch et al. (2005); Briggs et al. (2007); Dahm et al. (2007) and Alexander & Preibisch (2012). Since the PMS stars are in the magnetically saturated regime of late-type stars, one may reasonably expect their L_X/L_{bol} ratio to remain constant in time and $L_X - M$ to be simply a consequence of the mass-bolometric luminosity relation ($L_{bol} \propto M^\alpha$) coupled with the effect of the X-ray saturation. However, the $L_{bol} - M$ relationship for PMS stars is a strong function of time as the stars descend the convective Hayashi tracks (Siess et al. 2000).

Having the largest and most comprehensive IR/X-ray dataset of PMS stars at a wide range of ages allows us to consider if either of these two relationships ($L_X - L_{bol}$ or $L_X - M$) may remain unvarying (or slowly varying) with time during the early evolutionary phase of PMS stars. We transform the M_J, L_{bol}, and M outcome of the theoretical

evolutionary PMS models of Siess et al. (2000) onto an $M_J - \log(L_X)$ plane based on two different assumptions: $L_X - L_{bol}$ is fixed for all stars and evolutionary stages; and similarly $L_X - M$ is fixed for all stars and evolutionary stages. In the former case, the L_{bol} outcome of Siess et al. is substituted with L_X using the respective transformation from Telleschi et al. (2007), $\log(L_X) = 1.05 \times \log(L_{bol}/L_\odot) + 30.00$. In the latter case, the M outcome is substituted with L_X using the respective transformation from Telleschi et al. (2007), $\log(L_X) = 1.69 \times \log(M/M_\odot) + 30.33$. Figure 3 compares these two treatments with the Siess et al. (2000) isochrones. The top panel shows inconsistencies when constant $L_X - L_{bol}$ is assumed. Various MYStIX regions appear either younger than 0.5 Myr, older than 100 Myr, or have $M_J - \log L_X$ distributions that cross isochrones. The lower panel, where $L_X - M$ is assumed constant, shows much better consistency between models and data. Each MYStIX region distribution in the $M_J - \log L_X$ diagram roughly follows a reasonable theoretical PMS isochrone; for instance, the embedded Flame Nebula and W 40 regions are associated with the youngest isochrones ($t \simeq 0.5 - 1$ Myr; §7.2 and 7.3) while the isolated NGC 2362 cluster is associated with the oldest isochrones ($t \simeq 3 - 5$ Myr; §7.8).

Notice that Preibisch & Feigelson (2005) report the effect of the weak temporal evolution of X-ray luminosity during the first several Myr of PMS evolution, $L_X \propto t^{-1/3}$. We tested the impact of this possible effect on our inferred age estimates by modifying the shape of the Siess et al. (2000) model isochrones shown in Figure 3b with the following formula: $\log(L_X) = 30.33 + 1.69 \times \log(M/M_\odot) - 0.3 \times \log(t/t_0)$, where the fiducial t_0, as a typical age for both the Taurus and Orion regions, was varied between $[1.6 - 2]$ Myr. This effect is tiny for the young $\lesssim 2$ Myr regions, but produces systematically higher ages for older $\gtrsim 3$ Myr regions. However, for the oldest of the MYStIX regions, NGC 2362, these new age estimates become too high (over 5 Myr on the time scale of Siess et al. (2000), over 6 Myr on the time scale of Baraffe et al. (1998)) to be consistent with the published optical ages for NGC 2362 (§7.8). The effect is thus ignored from our further analyses.

The $L_X - L_{bol}$ and $L_X - M$ relationships are astrophysically poorly understood. One possibility consistent with the saturation limit is that X-ray luminosity scales with surface area because larger stars would allowi more flaring magnetic loops. Another possibility is that the X-ray activity scales with stellar volume allowing more opportunity for a convective dynamo. In both cases, the $L_X - M$ relation arises indirectly from the scaling of mass with radius. Finally, $L_X - M$ might reflect the early trapping of higher magnetic flux in more massive stars, although it seems unlikely that fully convective stars would be dominated by 'fossil' magnetic fields rather than by dynamo-generated fields. In any case, these astrophysical explanations could be too simplistic to reflect reality.

But even without clear scientific understanding for a universal $L_X - M$ for pre-main sequence stars, this relationship, when calibrated to the Taurus sample of Telleschi et al. (2007), has considerable predictive power. The use of poorly understood empirical relationships for calibrating other properties has a long tradition in astronomy: the Cepheid P-L relation of Leavitt & Pickering (1912), the $L \sim M^{3.5}$ relation for main sequence stars of Eddington (1924), the relations involving kinematics and luminosities in galaxies of Faber & Jackson (1976) and Tully & Fisher (1977), and the SN Ia light curve relation to L_{bol} widely used today (Hamuy et al. 1996).

3.2. Relationship between Age_{JX} and Absorption

Absorption plays an important role in Age_{JX} estimation. Both the J magnitude and the full-band X-ray luminosity are corrected for absorption for individual stars prior to their placement on the $L_X - M$ and $M_J - M$ diagrams. Note that these corrections may not be self-consistent. The J reddening correction is based on the NIR color-color diagram and physically arises from scattering and absorption by interstellar dust. The L_X absorption correction is based on the median energy of observed X-ray photons as a surrogate for soft

X-ray absorption by a column density of interstellar gas (Getman et al. 2010). We have chosen this divided approach, rather than a unified approach, to avoid assuming that the gas-to-dust ratio in interstellar clouds is fixed and known.

But absorption should also play an astronomical role that can help validate the median Age_{JX} estimates for MYStIX subclusters. We expect that older PMS stars will exhibit lower interstellar absorption than the youngest stars, which must reside in their natal dense molecular cores and filaments. As star formation progresses, older stars may kinematically drift from these obscured regions, cloud material can be depleted through conversion of gas to stars, and cloud material can be photoevaporated and ablated by the radiation and winds of newborn massive stars. A strict relationship between age and absorption is not expected due to variations in line-of-sight geometries and cloud star formation histories. Since the $J-H$ color index is a reddening indicator that is relatively insensitive to stellar spectral type or protoplanetary disk thermal emission, we expect stellar ages Age_{JX} to be anti-correlated with $J-H$.

We first consider the integrated sample of 5525 MPCM stars averaged over the full fields of MYStIX MSFRs. These fields are determined by the outline of single or mosaicked exposures of the *Chandra X-ray Observatory* and typically include a well-known rich OB-dominated stellar cluster plus subclusters, embedded young stars, and widely distributed young stars. Most regions have heterogeneous structures with stars ranging from lightly to heavily absorbed. Figure 4 shows the Age_{JX} vs. $J-H$ scatter diagram. Note that in the range of $(J-H) \lesssim 1.2$ mag, the spread in the J-H color is caused by the effect of absorption and the variation in the intrinsic colors of low-mass diskless stars, $(J-H)_0 \sim 0.6-0.7$ mag, and disk-bearing stars, $(J-H)_0 \sim 0.6-1.2$ mag. The bottom panel shows the similar scatter diagram using $A_V = A_J/0.28$ (Cardelli et al. 1989). Due to the wide spread in ages at a chosen absorption, a standard regression line does not give

an effective measure of this relationship. We apply instead the B-spline quantile regression described by He & Ng (1999) and implemented within the **R** statistical software system in CRAN package *CABS* (Ng & Maechler 2011). The spline fits for the 25%, 50% (median), and 75% quartiles to the Age_{JX} values as a function of the $J-H$ absorption indicator are shown in Figure 4. No monotonicity or concavity constraint is imposed, and 'spline knot' selection is based on the likelihood-based Akaike Information Criterion.

The median Age_{JX} regression relationship with $J-H$ is well approximated by two lines:

$$Age_{JX} = 4.00 - 1.71 \times (J-H) \text{ Myr} \quad \text{for } 0.5 < J-H < 1.7 \tag{1}$$

$$= 1.77 - 0.40 \times (J-H) \text{ Myr} \quad \text{for } 1.7 < J-H < 3.5 \tag{2}$$

These equations can be used for estimating cluster ages from $J-H$, provided that the bulk of the reddening is local to the cluster, i.e., local molecular cloud and circumstellar environments. A star with $J-H = 1.0$, for example, has an estimated age of $Age_{JX} = 2.3$ Myr. From the upper and lower quartile curves, we estimate that half of an ensemble of such stars would lie in the range $1.2-4.2$ Myr. A heavily absorbed star with $J-H = 3.0$ has estimated $Age_{JX} = 0.6$ Myr with interquartile range $0.4-1.4$ Myr. Clearly, the prediction for any single star is very uncertain.

The Age_{JX} *vs.* A_V relationship in Figure 4(b) favorably compares to a similar relationship recently obtained by Ybarra et al. (2013) from a disk fraction measurement calibrated to a disk evolution timescale and averaged over several clusters in the Rosette Molecular Cloud. These two age estimates agree well above $A_V > 5$ mag, but Ybarra gets older ages for $A_V \leq 5$ mag. The agreement at high absorption is gratifying given the very different approaches taken in the two studies. The difference at low absorption might be attributed to different methods for obtaining A_V; we estimate extinction by photometric dereddening as shown in Figure 2, while Ybarra et al. estimate A_V using a reduction in

background NIR star surface density. In any case, we note that the Ybarra et al. values lie within our 25%-to-75% interquartile MYStIX range, and thus the two estimates are in formal agreement even at low absorption.

As the scatter around the median regression line in Figure 4 is smaller, and the agreement with Ybarra et al. (2013) is better, for $J - H > 1.5$ mag, we use the regression lines at high absorption (equations 1 and 2 above) as a calibration for estimating ages of young, highly reddened subclusters. This is especially useful in cases of subclusters with poor Age_{JX} sampling. The calibration curve is thus employed as an alternative to the median Age_{JX} estimates for highly reddened MYStIX subclusters; these new estimates are called Age_{JH} in §4 and Table 2.

3.3. Uncertainties of Individual Stellar Ages

There are many sources of uncertainties in estimating ages of individual PMS stars. Here we ignore 'systematic' uncertainties that can globally shift age scales, such as errors in the distance to a MSFR or errors in the theoretical evolutionary tracks. The effects of distance uncertainties on the MYStIX age gradients resulted from our age analysis (§4.2) are further discussed in §5. We concentrate on possible sources of error in Age_{JX} that can produce scatter among age estimates of samples that are truly coeval.

For MYStIX stars, typical photometric errors on J-band magnitudes (mostly from UKIRT observations) are $\simeq 0.015$ mag. From a multi-epoch NIR study of nearby star forming regions, Scholz (2012) finds that in the J-band 'half the objects show variations of 5-20 per cent [0.05-0.2 mag]' and 'the other half is not variable'. Based on this work, we assume a typical scatter of $\Delta J \sim 0.1$ mag due to stellar variability. From the NIR color-color diagram (§2.3), the typical scatter of the $J - H$ color around the Taurus Locus

for the Taurus (above and below the locus) and the MYStIX (below the locus) stars is ~ 0.15 mag. This scatter is likely due to measurement errors, intrinsic imperfection of the locus, and to a lesser extent to abnormal individual extinction for some stars. This scatter of $\Delta(J-H) \sim 0.15$ mag is equivalent to the accuracy of source extinction of $\Delta A_V \sim 1.5$ mag. Thus, the reddening errors probably exceed or are comparable to the variability errors, which in turn exceed the photometric errors. For the majority of the stars treated here, this reddening uncertainty translates into uncertainties $\Delta Age_{JX} \leq 1$ Myr (Figure 1).

The Poisson noise and modeling uncertainties on L_X for the MYStIX Age_{JX} stars are about 0.2 dex each for typical MYStIX stars treated here (Broos et al. 2013). But the standard deviation of the residuals on the calibration $L_X - M$ diagram of Telleschi et al. (2007) is much larger with $\sigma_{\log(L_X)} = 0.4$ dex. Recall that multiple factors could contribute to this spread, including X-ray variability, binarity, possible suppression of X-rays by accretion, and intrinsic imperfection of a power law relationship. This scatter in $L_X - M$ corresponds to about 50% uncertainty in the mass estimation ($\sigma_M = 0.5 \times M$) which in turn propagates into $\sigma_t \sim 2$ Myr uncertainty on individual stellar ages (for a typical MYStIX star with mass around 0.8 $M_\odot$ and age around 2 Myr; Figure 1).

Thus, the individual age estimates are expected to be very uncertain, and wide scatter in individual Age_{JX} estimates should be present. Application of the $L_X - M$ transformation is likely the major source of the uncertainty. The age uncertainties are higher for more massive and/or older stars, but are lower for less massive and/or younger stars. For example, the stars we treat in the Orion Nebula Cluster (ONC) have median Age_{JX} (mass) of 1.6 Myr (0.6 $M_\odot$), and we expect $\sigma_t \sim 1$ Myr uncertainty on individual stellar ages. Formally, this is similar to the uncertainty on individual stellar ages that are reported for *Hubble Space Telescope* photometry and ground-based optical spectroscopy and photometry of stars in ONC (Reggiani et al. 2011): $\sigma_{log(t)} \sim 0.15$ dex for typical age values of 2.2 Myr.

It is critical to restate our objectives here. We are not principally interested in accurately evaluating individual stellar ages, or interested in the spread of the age distribution for an entire MSFR. Our principal interest is a 'typical' age value for spatially distinct subclusters within a MSFR. Rather than using the mean as an estimate of 'typical' age, we use the median value. The median has many advantages: it is robust to outliers and non-Gaussian scatter, invulnerable to the choice of logarithmic or other variable transformation, and is unaffected by a truncation at old ages seen in some regions[2].

We estimate an uncertainty for each subcluster median age using nonparametric 'bootstrap case resampling' (e.g., Wikipedia[3]; Davison & Hinkley 1997). This technique generates numerous sets of synthetic stellar ages by resampling with replacement from the observed stellar ages in a MYStIX subcluster and computing the median of each synthetic data set. The standard deviation of the ensemble of synthetic medians is then used as an estimate of the uncertainty of the median age. If the stellar ages in a subcluster are normally distributed, then this standard deviation represents a 68% confidence interval on the sample median.

A different well established technique for characterizing uncertainty on the median statistic, based on integrals of the binomial distribution (e.g., Conover 1980), can calculate a confidence level for any confidence interval whose end points lie at values found in the data set. Using this binomial technique, we made a second estimate for the uncertainty of our sample median by searching among the allowed confidence intervals for the one with the

[2]The evolutionary models used in our analysis stop at 5 Myr. Note that for any MYStIX subcluster, the number of 5 Myr old members is aways much lower than the number of < 5 Myr members, so the 'age saturation' effect at 5 Myr does not affect the estimate of the median age.

[3]`http://en.wikipedia.org/wiki/Bootstrapping_(statistics)`

smallest confidence level that exceeds 68%. For most MYStIX subclusters, the two error estimates differ by $< 35\%$.

We report the bootstrap errors as the uncertainties on subcluster ages in Table 2. These uncertainties are ~ 0.5 Myr for typical MYStIX subclusters ($N \sim 20$ stars with Age_{JX} estimates), which is often sufficiently accurate to discriminate age differences and gradients among subclusters. Richer subclusters naturally have smaller median age uncertainties.

3.4. Comparing Age_{JX} to Ages from Optical Data

The Age_{JX} estimates can be compared to age estimates independently derived from optical HRDs/CMDs. For this analysis, we choose the nearby and best studied MYStIX star forming regions, the Orion Nebula ($d = 414$ pc) and NGC 2264 ($d = 913$ pc), two of the most lightly absorbed MSFRs in the MYStIX survey.

For the Orion Nebula, optical ages are obtained from Da Rio et al. (2010) where they were computed by transforming measurements onto the HRD and applying the Siess et al. (2000) PMS tracks. T_{eff} and L_{bol} values were derived from ground-based optical $UBVI$ and TiO-band photometry and spectroscopy. Their detailed analysis includes construction of synthetic spectra for 2 Myr Siess models to estimate bolometric corrections, derivation of some spectral types from TiO indices, and corrections for reddening and accretion luminosity. Da Rio et al. also use a distance of 414 pc to the region. The Da Rio et al. analysis results in a broad range of ages with most Orion stars lying between 0.3 and 10 Myr with a peak at $2 - 3$ Myr. The age dispersion is present for all stellar masses. We compare Age_{JX} and the Da Rio et al. ages for 263 stars in common between the two samples.

For NGC 2264, the optical data are obtained from Mayne et al. (2007) who compute ages from the V *vs.* $V - I$ CMD. Their sample is a union of PMS members obtained from

proper motion, X-ray, Hα, periodic variability, and radial velocity surveys. Their sample is then truncated to a lightly absorbed stellar sub-sample with $J - H < 1$ mag. Mayne et al. compare their observed CMD to the model predictions of Siess et al. (2000) and obtain a collective age $\simeq 3$ Myr with some age spread. Since Mayne et al. do not report individual ages and their assumed distance to the region of 832 pc differs from our assumed distance of 913 pc, here we recalculate optical ages using their optical VI_C photometry data. The optical photometric ages are computed assuming the uniform source extinction for the lightly-absorbed stellar sample of $A_V = 0.22$ mag (Dahm 2005) and the reddening law of $A_I/A_V = 0.6$ (Bessell & Brett 1988). The comparison sample with optical and Age_{JX} age estimates in NGC 2264 has 152 stars.

Figure 5 plots the Age_{JX} against the ages derived from the optical HRD (Orion) or CMD (NGC 2264); agreement would distribute the stars along the dashed lines. The discrimination between diskless and disk-bearing stars is based on the analysis of Povich et al. (2013) for NGC 2264 and Megeath et al. (2012) for Orion. In all four panels, the correlation between the Age_{JX} and optical ages is statistically significant based on Kendall's τ nonparametric measure of bivariate correlation with $\tau \simeq 0.35$ for NGC 2264 and $\tau \simeq 0.17$ for the Orion Nebula.

But the agreement between the two age estimates for many individual stars is generally poor with dispersion at any chosen age only slightly smaller than that present in the full sample. These large spreads are likely due to the poor age estimates for individual stars from optical (e.g., Reggiani et al. 2011) and MYStIX (§3.3) data. The greater scatter at older ages is due to the smaller M_J ($\log(L_{bol})$) separation of older isochrones and thus the higher age uncertainties for older stars. Only small offsets in the medians of stellar ages are seen for the sample of all NGC 2264 stars and the sample of mainly diskless Orion stars. We have checked to ensure that different assumed extinction laws, the $A_J/A_{K_s} = 2.65$

choice of Megeath et al. (2012) versus our choice of $A_J/A_{K_s} = 2.5$ (Indebetouw et al. 2005), have a negligible effect on the dispersion or bias in the scatter diagram for the disk-bearing Orion stars.

The comparison between Age_{JX} and optical ages changes with different methods, assumptions for source extinction, and catalogs (published versus new unpublished optical catalogs). There are ways to improve the optically-derived ages (N. Da Rio, private communication). No clear scientific conclusion can be inferred from the poor association between our new age estimator and traditional HRD- and CMD-based age estimators. If there was confidence that Age_{opt} values were accurate, then we would infer that Age_{JX} values were not useful. But, as discussed in §3.3, both Age_{JX} and Age_{opt} values for individual stars are inaccurate (see also §5). The only conclusion we can draw from Figure 5 is that inferences based on stellar ages, such as age spreads within clusters and age gradients across star formation complexes, may differ when Age_{JX} rather than Age_{opt} values are used. However, most MYStIX MSFRs suffer too much obscuration for optical photometry and spectroscopy, so Age_{opt} estimates can not be readily obtained for our sample.

4. Ages of MYStIX Regions and subclusters

4.1. Overview

Figure 6 shows boxplots of the Age_{JX} distributions for the 15 MYStIX regions under consideration. The 'box' indicates the 25%, 50% (median), and 75% quartiles with 'whiskers' set at 1.5 times the interquartile range. Points lying beyond these values are plotted individually as outliers; a Gaussian distribution would have few outliers. The notches around the median approximate the confidence intervals of the median. The box width is scaled to the square root of the sample size. Recall that older ages are all set to be

5 Myr.

All MYStIX regions show wide age distributions. Some distinction between regions can be discerned: W 40 and Flame Nebula are youngest (medians < 1.0 Myr) while Rosette Nebula, Carina Nebula, and NGC 2362 are oldest (medians > 3.0 Myr). But the interquartile ranges of even these extreme cases greatly overlap. Much of this dispersion is undoubtedly due to the diverse environments in these fields. The Rosette Nebula fields, for example, have embedded clusters as well as the main revealed cluster (Wang et al. 2010). The Carina Nebula has both embedded groups in the South Pillars and the older cluster Tr 15 and thousands of older dispersed stars (Townsley et al. 2011). Figure 4 shows that stars drawn from a range of absorptions − revealed and embedded clusters − will exhibit a wide range of ages. In our view, the study of ages averaged over the full MYStIX regions (as shown in Figure 6) is not a fruitful enterprise.

We instead follow the lead of Kuhn et al. (2014) who have divided the MPCM population into spatially distinct clusters using an objective statistical algorithm. A 'finite mixture model' composed of multiple isothermal ellipsoidal clusters and an unclustered population is fit to the two-dimensional positions of MPCM stars. Each subcluster component has six parameters (right ascension, declination, core radius, central stellar density, ellipticity, and ellipse orientation angle) and the fit is found by maximizing the likelihood of the parameters. The number of clusters in a MYStIX region is chosen by maximizing the penalized likelihood Akaike Information Criterion assisted, in some cases, with minimizing extrema in smoothed residual maps. The mixture model is then used as a 'soft classifier' that, with additional decision rules, allows individual MPCM stars to be assigned to the clusters and to the unclustered component.

Table 2 presents some of the cluster properties for over a hundred subclusters (denoted "A", "B", ...) and unclustered or ambiguous components (denoted "U") found by

Kuhn et al. (2014) in 15 MYStIX MSFRs[4]. Each subcluster component is assigned an age (column 11), defined as the median Age_{JX} of the stellar members of the component. The uncertainties shown for the median ages are symmetric 68% confidence intervals estimated by bootstrap resampling (§3.3). Age_{JX} values in column (11) are oomitted when the subcluster is very sparse with $< 3-5$ members that satisfy the criteria for Age_{JX} analysis (§2.2). For 40 highly reddened subclusters with $(J-H)_{tot} > 1.5$ mag, column (12) lists the Age_{JH} estimated from the spline fit to the *Age vs.* $(J-H)$ data given by equations (1)-(2) in § 3.2. These Age_{JH} estimates are fairly consistent with the Age_{JX} estimates obtained from the median of individual star members of the subcluster shown in column (11). For 21 sub-clusters with both age estimates, there is only a small bias $(Age_{JX} - Age_{JH}) = 0.2$ Myr and a dispersion of only 0.3 Myr.

For the Orion Nebula, Flame Nebula, and M 17 MSFRs, we also investigate age estimates for additional groups of stars defined by combining or subdividing Kuhn et al. (2014) clusters. The respective results on these special age estimates are given in the current paper for M 17 (§7.13) and in a companion paper for Orion and Flame (Getman et al. 2014).

4.2. Principal Results

The importance of the subcluster median ages becomes apparent when we compare them to their spatial locations and absorptions in Figures 7 - 22. Here we summarize several broad and powerful results evident from the figures. A detailed discussion of each MYStIX region is given in the Appendix. These are the main findings of this study.

[4]Five regions are omitted due to the poor Age_{JX} sampling of MYStIX subclusters: RCW 38, W 3, W 4, Trifid Nebula, and NGC 3576.

1. In most MYStIX regions, we see an anti-correlation between median Age_{JX} and median $J - H$ for the subclusters. This is expected from the individual star results shown in Figure 4 and validates the expected trend that younger subclusters are more embedded in molecular material than older subclusters.

2. In all MYStIX regions, the unclustered population (shown as magenta symbols in Figures 7 - 22) is older than most of the subcluster populations. This is most clearly seen in regions with a single dominant cluster: Flame Nebula, W 40, and RCW 36. This is readily interpreted as the kinematic dispersion of older generations of stars formed in the molecular cloud. We infer that MYStIX regions have been forming stars for millions of years before the compact rich clusters we see today were formed.

3. In some MYStIX regions, a coherent spatial gradient in subcluster ages is seen, consistent with the progression of star formation through the molecular cloud on scales of several parsecs. This is most clearly seen in the Rosette Nebula, Eagle Nebula, NGC 6634, and NGC 1893. For a typical region extent of ~ 10 pc and age gradient of ~ 2 Myr, we infer a characteristic 'speed' of 5 km s^{-1} for the propagation of star formation through a giant molecular cloud.

4. In other cases, the subclusters have indistinguishable ages, or have distinct ages in an incoherent spatial pattern. This is seen in the Orion Nebula, NGC 2264, Lagoon Nebula, NGC 2362, DR 21, NGC 6357, M 17, and the Carina Nebula. A few examples follow. The three clusters producing H II regions in NGC 6357 appear to be coeval. Cluster formation along the DR 21 filament, about 5 parsecs in length, appears roughly simultaneous. The subclusters superposed on Carina South Pillars show a broad (possibly bimodal) range of ages; this could be from contamination by the old distributed population and/or could be consistent with scenarios of triggered star formation proceeding in these clouds for millions of years (Povich et al. 2011). On

occasion, a lightly absorbed cluster (or its portion) lies projected against a region harboring embedded clusters: the subcluster K in front of the IRS 1 cloud in NGC 2264, the subcluster L in front of the Rosette Molecular Cloud, and the Orion Nebula Cluster in front of OMC-1.

5. Advantages and Limitations of Age_{JX} Analysis

The use of Age_{JX} values based on J and L_X measurements, rather than other age methods such as an HRD or a CMD derived from visual band observations, is potentially advantageous for a number of reasons:

1. Age_{JX} estimates can be made for young stars over a wide range of PMS evolutionary stages and cloud absorptions. Infrared-only studies, biased towards selection of disk-bearing YSOs, are typically restricted to the earlier stages, while optical-only studies are typically restricted to later, lightly-obscured stages.

2. Compared to optical and mid-infrared surveys where diffuse nebular emission from ionized gas and heated polycyclic aromatic hydrocarbons can be bright, X-ray and NIR are subject to less confusion from nebular emission by heated gas and dust.

3. Extinction corrections are much smaller in the J-band than V-band; recall that $A_J = 0.28A_V$. Both X-ray and NIR surveys penetrate comparably deeper into obscuring material than optical surveys. This gives a major advantage to Age_{JX} estimates in MYStIX MSFRs where absorption can vary by tens of magnitudes between subclusters and individual stars.

4. Multi-epoch photometric surveys have shown that the NIR bands are less affected by variability compared to optical bands. Photometric variability can arise either from

changes in accretion rates or from magnetic activity. There will be thus less scatter in estimating intrinsic photospheric luminosities from single-epoch J photometry in contrast to single-epoch V photometry often used in HRD/CMD studies. Herbst et al. (1994) find that the photometric variability of classical T Tauri stars decreases in amplitude $>$ 2-fold from V to I bands. Frasca et al. (2009) find that photometric effects of rotationally modulated spots are typically $\Delta J \simeq 0.06$ mag, several times lower than in the V band. Similarly, Goulding et al. (2012) recommend the J band for planetary transit surveys in magnetically active M dwarfs. From a near-infrared study of nearby star forming regions, Scholz (2012) conclude that 'the variability in the J-band is less than 0.5 mag for the overwhelming majority of YSOs, i.e. a factor of $<$ 1.6 in luminosity, which is only a minor part of the observed spread in the HR diagrams'.

5. Unlike optical measurements, the X-ray luminosity L_X from most MSFRs is not detectably affected by accretion variations or emission from accretion shocks. The soft X-rays from the accretion shock is generally lost due to interstellar absorption. No causal link is seen between the sources of optical variability (often accretion related) and X-ray variability (Stassun et al. 2006). X-ray variability is equally ubiquitous on both diskless and disk-bearing stars and is mainly due to magnetic activity (Wolk et al. 2005; Stelzer et al. 2007; Getman et al. 2008). The contribution of the 'very soft' X-ray emission from accretion shocks can only be detected (and modeled) in cases where there is negligible soft X-ray absorption, which is not the case for most MSFRs. However, although independent of accretion, the X-ray variability does affect the Age_{JX} estimates, as detailed in §3.3.

6. Cluster ages are often estimated from infrared excess properties. In some studies, disk-bearing stars are binned into a classification scheme (Class 0, I, and II young stellar

objects) that does not have an established calibration to stellar age. In other studies, the disk fraction is measured (often with a poorly established sample of disk-free stars) and ages are estimated from a rough calibration curve (Hernández et al. 2008; Mamajek 2009). Nevertheless, the age vs. disk fraction calibration of Ybarra et al. (2013) seems consistent with the Age_{JX} estimates for the highly-absorbed MPCMs (§3.2).

7. Unlike some studies where different age estimation methods are applied to arbitrarily defined regions or (sub)samples, Age_{JX} values are calculated for stellar samples within subclusters defined by a mathematically objective procedure in Kuhn et al. (2014).

8. Unlike some studies where cluster ages are the mean of age or log-age distributions, Age_{JX} results reported here are calculated using median values that are robust to non-Gaussianity and unaffected by transformation of the age variable.

9. Our homogeneous Age_{JX} analysis is applied to a large number of star forming regions, whereas most previous studies applied different methods to different regions. The Age_{JX} estimates for over a hundred MYStIX subclusters are referenced to a uniform time scale, which depends on the Siess et al. (2000) models and the adopted distances to the MYStIX regions. This allows reasonably reliable comparison of star formation histories within and between MSFRs. Our median Age_{JX} estimates for MYStIX subclusters are listed in Table 2.

However, like most of the other age methods, the Age_{JX} method is prone to some problems and limitations:

1. Our Age_{JX} estimates for individual stars are highly uncertain. The largest contribution to the error is the scatter on the $L_X - M$ diagram that causes typical Age_{JX} uncertainties of ~ 2 Myr (§3.3). However, scatter of similar amplitude is seen

in optically derived ages (§3.4); this is the well-known problem of age spreads in young stellar clusters. We use the robust median estimator that effectively reduces both the influence of outliers and individual star age uncertainties in estimating subcluster ages.

2. For some embedded MYStIX subclusters the inferred Age_{JX} or Age_{JH} estimates may overestimate true ages due to the poor sensitivity of the Age_{JX} method to very young Class 0/I protostars.

3. Our Age_{JX} estimates for the individual MYStIX stars, and hence the median values for subclusters, have not been corrected for possible effects of binarity. True ages may thus be somewhat older than we state. This deficiency is shared with most other age estimates at distances of MSFRs.

4. Any anomalous dust extinction laws characteristic of some obscured regions of molecular clouds are ignored.

5. Age_{JX} relies on the $L_X - M$ regression averaged between accreting and non-accreting stars that are known to have different X-ray luminosity functions (§3.1). The accreting stars are on average less X-ray active. But we do not recommend use of the separate regression lines reported by Telleschi et al. (2007) for a number of reasons. First, for the typical mass range of the MYStIX Age_{JX} stars, the recent published results on the presence/absence of the effect are controversial (§3.1). Second, a clear separation between accreting and non-accreting systems is not available for most MYStIX MSFRs. Third, the XPHOT method for estimating L_X is based on the X-ray emission models already averaged between accreting and non-accreting systems (Getman et al. 2010).

6. As for any other age method, our age estimates are prone to changes as the distance

estimate to a star forming region varies. Figure 23 exemplifies the effect of uncertain distances on the MYStIX age gradients. Following are a few notable examples of this effect.

First, changes in distance estimates will globally shift inferred age scales with larger distances resulting in younger age scales. Second, due to the non-uniform separation and orientation of the theoretical isochrones on the M_J versus M diagram (Figure 1) and the distance dependence of both M_J and M (through L_X) quantities, the slopes on the median(Age_{JX}) vs. median($J-H$) plots would generally change with the changing reference distance. Third, distance uncertainties of $\sim 5\%$ (Feigelson et al. 2013, Table 1) propagate into subcluster age differences of only a few to several percent (e.g., Orion, Rosette, and NGC 1893 in Figure 23). Distance uncertainties of $\sim 30-40\%$, as seen in RCW 38 and the Lagoon Nebula, propagate into subcluster age differences of $\sim 20-50\%$. Finally, different distances to subclusters within the same MYStIX region would likely have negligible effect on the inferred age gradients in the region. For instance, using volumetric assumptions for the nearly circular NGC 1893 and Rosette bubbles, it is reasonable to suggest that distance differences to the MYStIX subclusters in these regions of $\sim 10-20$ pc are only $0.3-2\%$ of the total distance to the region and give no more than a few percent difference in inferred subcluster ages.

6. Conclusions

Researchers have historically used a number of different methods for dating young stellar clusters: isochrone fitting on the HRD or on photometric CMD, protoplanetary disk fraction, lithium depletion, and other procedures (Mamajek et al. 2009; Soderblom 2010; Jeffries 2012). The placement of PMS stars on the HRD or CMD with theoretical

evolutionary isochrones is probably the most popular method in the literature for dating young ($\lesssim$ 10 Myr) clusters but the individual stellar ages are highly uncertain. The distributions of stellar ages within rich clusters and across large-scale MSFRs often show wide age spreads; it has been unclear whether this is entirely due to poor individual age estimates or to real extended star formation histories.

The problem of age estimation in MSFRs is particularly challenging, as reliable censuses of stellar members are hard to obtain and complex star formation histories are likely to be present. The MYStIX project has produced rich samples in 20 OB-dominated young star forming regions at distances < 4 kpc using sensitive X-ray, NIR, and mid-infrared photometric catalogs (Feigelson et al. 2013). Kuhn et al. (2014) has segmented the spatial distribution of MYStIX Probable Cluster Members into dozens of distinct subclusters. Some subclusters are deeply embedded in cloud material and have mostly disk-bearing stars, while others have low obscuration and mostly disk-free stars. The MYStIX sample thus provides a valuable opportunity to characterize star formation histories in MSFRs where optical or NIR spectroscopy is as yet unavailable.

In this work, we develop a new PMS stellar age estimator, Age_{JX}, based on J-band stellar photospheric emission and on X-ray emission from coronal magnetic flaring. Stellar masses are directly derived from absorption-corrected X-ray luminosities using the $L_X - M$ relation from the Taurus cloud. These masses are combined with J-band magnitudes, corrected for source extinction and distance, for comparison with PMS evolutionary models (Siess et al. 2000) to estimate ages. We provide a homogeneous set of median Age_{JX} for over a hundred subclusters identified by Kuhn et al. (2014, Table 2). The method has a number of advantages over traditional methods of age estimation for young stellar clusters (§5).

The main conclusions of our study are as follows:

1. We demonstrate that the $L_X - M$ relation, rather than the L_X/L_{bol} ratio, remains slowly varying during the early PMS phase (§3.1).

2. The Age_{JX} stellar ages are anticorrelated with the source extinction A_V and the $J-H$ color. At high absorptions, the $Age_{JX} - A_V$ relationship is consistent with that of Ybarra et al. (2013) that was independently derived using disk fraction techniques. The Age_{JX} vs. $J-H$ trend can serve as an approximate age predictor for young, highly reddened clusters, provided that the bulk of the reddening is local to the clusters (§3.2).

3. To overcome the dispersion of highly uncertain individual ages, we compute median ages (and their confidence intervals) of stellar samples within subclusters defined by the companion study of Kuhn et al. (2014) (§§4 and 7). We find narrowly constrained ages for these spatially distinct structures. Thus, we establish that (at least some) of the apparent age spread in MSFRs is real and can be attributed to clusters formed at different times.

4. Spatial gradients in subcluster ages are often seen, consistent with astronomically reasonable patterns of star formation histories with older lightly absorbed structures on one side, younger heavily absorbed structures on the other side, and intermediate-age structures in between. Some regions do not show coherent star formation patterns. However, widely distributed populations nearly always have older ages than the principal clusters. The progression of star formation within a MSFR can be traced over spatial scales of several parsecs and time scales of several million years. Patterns of star formation histories can be compared between MSFRs. We caution that uncertainties in distance to MYStIX MSFRs can cause systematic shifts in the age scales (§5).

We thank R. Jeffries (Keele University), T. Megeath (University of Toledo), and N. Da Rio (ESA) for useful comments. We also thank the anonymous referee for his time and useful comments that improved this work. The MYStIX project is supported at Penn State by NASA grant NNX09AC74G, NSF grant AST-0908038, and the *Chandra* ACIS Team contract SV474018 (G. Garmire & L. Townsley, Principal Investigators), issued by the *Chandra* X-ray Center, which is operated by the Smithsonian Astrophysical Observatory for and on behalf of NASA under contract NAS8-03060. The Guaranteed Time Observations (GTO) included here were selected by the ACIS Instrument Principal Investigator, Gordon P. Garmire, of the Huntingdon Institute for X-ray Astronomy, LLC, which is under contract to the Smithsonian Astrophysical Observatory; Contract SV2-82024. This research made use of data products from the *Chandra* Data Archive and the *Spitzer Space Telescope*, which is operated by the Jet Propulsion Laboratory (California Institute of Technology) under a contract with NASA. The United Kingdom Infrared Telescope is operated by the Joint Astronomy Centre on behalf of the Science and Technology Facilities Council of the U.K. This work is based in part on data obtained as part of the UKIRT Infrared Deep Sky Survey and in part on data obtained in UKIRT director's discretionary time. This research used data products from the Two Micron All Sky Survey, which is a joint project of the University of Massachusetts and the Infrared Processing and Analysis Center/California Institute of Technology, funded by the National Aeronautics and Space Administration and the National Science Foundation. This research has also made use of NASA's Astrophysics Data System Bibliographic Services and SAOImage DS9 software developed by Smithsonian Astrophysical Observatory.

Facilities: CXO (ASIS), Spitzer (IRAC), CTIO:2MASS (), UKIRT (WFCAM).

REFERENCES

Alexander, F., & Preibisch, T. 2012, A&A, 539, A64

Ascenso, J., Alves, J., Vicente, S., & Lago, M. T. V. T. 2007, A&A, 476, 199

Baraffe, I., Chabrier, G., Allard, F., & Hauschildt, P. H. 1998, A&A, 337, 403

Baraffe, I., Chabrier, G., & Gallardo, J. 2009, ApJ, 702, L27

Baxter, E. J., Covey, K. R., Muench, A. A., et al. 2009, AJ, 138, 963

Bessell, M. S., & Brett, J. M. 1988, PASP, 100, 1134

Bouvier, J. 2013, in *Role and Mechanisms of Angular Momentum Transport During the Formation and Early Evolution of Stars*, EAS Pub. Ser. 62, 143

Briggs, K. R., Güdel, M., Telleschi, A., et al. 2007, A&A, 468, 413

Broos, P. S., Feigelson, E. D., Townsley, L. K., et al. 2007, ApJS, 169, 353

Broos, P. S., Getman, K. V., Povich, M. S., et al. 2013, ApJS, 209, 32

Caramazza, M., Micela, G., Prisinzano, L., et al. 2008, A&A, 488, 211

Cardelli, J. A., Clayton, G. C., & Mathis, J. S. 1989, ApJ, 345, 245

Chini, R., & Hoffmeister, V. 2008, Handbook of Star Forming Regions, Volume II, 625

Conover, W. J. 1980, Practical Nonparametric Statistics, John Wiley and Sons, New York, ISBN-10: 0471028673

Da Rio, N., Robberto, M., Soderblom, D. R., et al. 2010, ApJ, 722, 1092

Dahm, S. E. 2005, AJ, 130, 1805

Dahm, S. E., Simon, T., Proszkow, E. M., & Patten, B. M. 2007, AJ, 134, 999

Dahm, S. E. 2008, Handbook of Star Forming Regions, Volume I, 966

Dahm, S. E. 2008, Handbook of Star Forming Regions, Volume II, 26

Davison, A. C., Hinkley, D. V. 1997, Bootstrap Methods and their Application, Cambridge Series in Statistical and Probabilistic Mathematics, ISBN-10: 0521574714

Eddington, A. S. 1924, MNRAS, 84, 308

Eggenberger, P., Haemmerlé, L., Meynet, G., & Maeder, A. 2012, A&A, 539, A70

Ellerbroek, L. E., Bik, A., Kaper, L., et al. 2013, A&A, 558, 102

Faber, S. M., & Jackson, R. E. 1976, ApJ, 204, 668

Fang, M., van Boekel, R., King, R. R., et al. 2012, A&A, 539, A119

Feigelson, E. D., Casanova, S., Montmerle, T., & Guibert, J. 1993, ApJ, 416, 623

Feigelson, E. D., Martin, A. L., McNeill, C. J., Broos, P. S., & Garmire, G. P. 2009, AJ, 138, 227

Feigelson, E. D., Getman, K. V., Townsley, L. K., et al. 2011, ApJS, 194, 9

Feigelson, E. D., & Babu, G. J. 2012, Modern Statistical Methods for Astronomy, Cambridge, UK: Cambridge University Press

Feigelson, E. D., Townsley, L. K., Broos, P. S., et al. 2013, ApJS, 209, #26

Flaccomio, E., Micela, G., & Sciortino, S. 2006, A&A, 455, 903

Frasca, A., Covino, E., Spezzi, L., et al. 2009, A&A, 508, 1313

Friedman, J. H. 1984, A variable span scatterplot smoother. Laboratory for Computational Statistics, Stanford University Technical Report No. 5.

Getman, K. V., Flaccomio, E., Broos, P. S., et al. 2005, ApJS, 160, 319

Getman, K. V., Feigelson, E. D., Townsley, L., et al. 2006, ApJS, 163, 306

Getman, K. V., Feigelson, E. D., Micela, G., et al. 2008, ApJ, 688, 437

Getman, K. V., Feigelson, E. D., Luhman, K. L., et al. 2009, ApJ, 699, 1454

Getman, K. V., Feigelson, E. D., Broos, P. S., Townsley, L. K., & Garmire, G. P. 2010, ApJ, 708, 1760

Getman, K. V., Feigelson, E. D., & Kuhn, M. A. 2014, ApJ, accepted, (#ApJ93628)

Goulding, N. T., Barnes, J. R., Pinfield, D. J., et al. 2012, MNRAS, 427, 3358

Grosso, N., Feigelson, E. D., Getman, K. V., et al. 2005, ApJS, 160, 530

Guarcello, M. G., Damiani, F., Micela, G., et al. 2010, A&A, 521, A18

Guarcello, M. G., Micela, G., Peres, G., Prisinzano, L., & Sciortino, S. 2010, A&A, 521, A61

Güdel, M., Briggs, K. R., Arzner, K., et al. 2007, A&A, 468, 353

Güdel, M., & Telleschi, A. 2007, A&A, 474, L25

Haisch, K. E., Jr., Lada, E. A., & Lada, C. J. 2001, ApJ, 553, L153

Hamuy, M., Phillips, M. M., Suntzeff, N. B., et al. 1996, AJ, 112, 2391

He, X., & Ng, P. 1999, COBS: Qualitatively Constrained Smoothing via Linear Programming; Computational Statistics 14, 315-337

Herbst, W., Herbst, D. K., Grossman, E. J., & Weinstein, D. 1994, AJ, 108, 1906

Hernández, J., Hartmann, L., Calvet, N., et al. 2008, ApJ, 686, 1195

Ng, P. T., & Maechler, M. 2011, cobs: COBS Constrained B-Splines (Sparse matrix based), R package version 1.2-2, `http://CRAN.R-project.org/package=cobs`

Hill, T., Motte, F., Didelon, P., et al. 2012, A&A, 542, A114

Hillenbrand, L. A. 1997, AJ, 113, 1733

Hoffmeister, V. H., Chini, R., Scheyda, C. M., et al. 2008, ApJ, 686, 310

Indebetouw, R., Mathis, J. S., Babler, B. L., et al. 2005, ApJ, 619, 931

Indebetouw, R., Robitaille, T. P., Whitney, B. A., et al. 2007, ApJ, 666, 321

Jeffries, R. D., Littlefair, S. P., Naylor, T., & Mayne, N. J. 2011, MNRAS, 418, 1948

Jeffries, R. D. 2012, Star Clusters in the Era of Large Surveys, Springer, 163

King, R. R., Naylor, T., Broos, P. S., Getman, K. V., & Feigelson, E. D. 2013, ApJS, 209, #28

Kuhn, M. A., Getman, K. V., Feigelson, E. D., et al. 2010, ApJ, 725, 2485

Kuhn, M. A., Getman, K. V., Broos, P. S., Townsley, L. K., & Feigelson, E. D. 2013a, ApJS, 209, #27

Kuhn, M. A., Povich, M. S., Luhman, K. L., et al. 2013b, ApJS, 209, #29

Kuhn, M. A.. Feigelson, E. D., Getman, K. V., Baddeley, A. J., Townsley, L. K., Broos, P. S., Sills, A., Bate, M. R., Povich, Luhman, K. L., Busk, H. A., Naylor, T. & King, R. R. 2014, ApJ, submitted and under revision

Kumar, M. S. N., Davis, C. J., Grave, J. M. C., Ferreira, B., & Froebrich, D. 2007, MNRAS, 374, 54

Kumar, D. L., & Anandarao, B. G. 2010, MNRAS, 407, 1170

Lada, C. J., Muench, A. A., Haisch, K. E., Jr., et al. 2000, AJ, 120, 3162

Leisawitz, D., Bash, F. N., & Thaddeus, P. 1989, ApJS, 70, 731

Levine, J. L., Steinhauer, A., Elston, R. J., & Lada, E. A. 2006, ApJ, 646, 1215

Leavitt, H. S., & Pickering, E. C. 1912, Harvard College Observatory Circular, 173, 1

Luhman, K. L., Allen, P. R., Espaillat, C., Hartmann, L., & Calvet, N. 2010, ApJS, 186, 111

Mamajek, E. E. 2009, in *Exoplanets and Disks: Their Formation and Diversity*, AIP Conf. 158, 3, Institute of Physics Conference Series, 1158, 3

Mamajek, E. E., Soderblom, D. R., & Wyse, R. F. G. (eds.) 2009, *The Ages of Stars*, IAU Symposium #258, Cambridge University Press

Mayne, N. J., Naylor, T., Littlefair, S. P., Saunders, E. S., & Jeffries, R. D. 2007, MNRAS, 375, 1220

Megeath, S. T., Gutermuth, R., Muzerolle, J., et al. 2012, AJ, 144, 192

Meyer, M. R., Flaherty, K., Levine, J. L., et al. 2008, Handbook of Star Forming Regions, Volume I, 662

Muench, A., Getman, K., Hillenbrand, L., & Preibisch, T. 2008, Handbook of Star Forming Regions, Volume I, 483

Naylor, T. 2009, MNRAS, 399, 432

Naylor, T., Broos, P. S., & Feigelson, E. D. 2013, ApJS, 209, #30

Neuhaeuser, R., Sterzik, M. F., Schmitt, J. H. M. M., Wichmann, R., & Krautter, J. 1995, A&A, 297, 391

O'dell, C. R. 2001, ARA&A, 39, 99

Oliveira, J. M. 2008, Handbook of Star Forming Regions, Volume II, 599

Pandey, A. K., Samal, M. R., Chauhan, N., et al. 2013, New A, 19, 1

Persi, P., & Tapia, M. 2008, Handbook of Star Forming Regions, Volume II, 456

Pettersson, B. 2008, Handbook of Star Forming Regions, Volume II, 43

Piau, L., & Turck-Chièze, S. 2002, ApJ, 566, 419

Povich, M. S., Churchwell, E., Bieging, J. H., et al. 2009, ApJ, 696, 1278

Povich, M. S., Smith, N., Majewski, S. R., et al. 2011, ApJS, 194, 14

Povich, M. S., Kuhn, M. A., Getman, K. V., et al. 2013, ApJS, 209, #31

Preibisch, T., & Feigelson, E. D. 2005, ApJS, 160, 390

Preibisch, T., Kim, Y.-C., Favata, F., et al. 2005, ApJS, 160, 401

Preibisch, T., Ratzka, T., Kuderna, B., et al. 2011, A&A, 530, A34

Preibisch, T. 2012, Research in Astronomy and Astrophysics, 12, 1

Prisinzano, L., Micela, G., Flaccomio, E., et al. 2008, ApJ, 677, 401

Prisinzano, L., Sanz-Forcada, J., Micela, G., et al. 2011, A&A, 527, A77

Prisinzano, L., Micela, G., Sciortino, S., Affer, L., & Damiani, F. 2012, A&A, 546, A9

Reggiani, M., Robberto, M., Da Rio, N., et al. 2011, A&A, 534, A83

Reipurth, B., & Schneider, N. 2008, Handbook of Star Forming Regions, Volume I, 36

Roccatagliata, V., Bouwman, J., Henning, T., et al. 2011, ApJ, 733, 113

Román-Zúñiga, C. G., & Lada, E. A. 2008, Handbook of Star Forming Regions, Volume I, 928

Russeil, D., Zavagno, A., Motte, F., et al. 2010, A&A, 515, A55

Siess, L., Dufour, E., & Forestini, M. 2000, A&A, 358, 593

Scholz, A. 2012, MNRAS, 420, 1495

Smith, N., & Brooks, K. J. 2008, Handbook of Star Forming Regions, Volume II, 138

Soderblom, D. R. 2010, ARA&A, 48, 581

Stassun, K. G., van den Berg, M., Feigelson, E., & Flaccomio, E. 2006, ApJ, 649, 914

Stelzer, B., Flaccomio, E., Briggs, K., et al. 2007, A&A, 468, 463

Stelzer, B., Preibisch, T., Alexander, F., et al. 2012, A&A, 537, A135

Telleschi, A., Güdel, M., Briggs, K. R., Audard, M., & Palla, F. 2007, A&A, 468, 425

Tothill, N. F. H., Gagné, M., Stecklum, B., & Kenworthy, M. A. 2008, Handbook of Star Forming Regions, Volume II, 533

Townsley, L. K., Broos, P. S., Corcoran, M. F., et al. 2011, ApJS, 194, 1

Townsley, L. K., Broos, P. S., Garmire, G. P. 2013, ApJS, submitted

Tully, R. B., & Fisher, J. R. 1977, A&A, 54, 661

Wang, J., Townsley, L. K., Feigelson, E. D., et al. 2007, ApJS, 168, 100

Wang, J., Feigelson, E. D., Townsley, L. K., et al. 2010, ApJ, 716, 474

Wang, J., Feigelson, E. D., Townsley, L. K., et al. 2011, ApJS, 194, 11

Wolk, S. J., Harnden, F. R., Jr., Flaccomio, E., et al. 2005, ApJS, 160, 423

Ybarra, J. E., Lada, E. A., Román-Zúñiga, C. G., et al. 2013, ApJ, 769, 140

7. Appendix: Age_{JX} Results for Individual Massive Star Forming Regions

7.1. Orion Nebula

The Orion Nebula Cluster (ONC) produces the nearest ($D \sim 414$ pc) unobscured H II region, lying in front of the OMC 1 (Orion Molecular Cloud core #1) molecular filament tracing the central ridge of the Orion A cloud. For detailed description of the region see O'dell (2001); Muench et al. (2008, and references therein). Based on *Chandra* X-ray (Getman et al. 2005) and *Spitzer* mid-infrared surveys (Megeath et al. 2012), over 1500 MPCMs are identified as likely members of the region (Broos et al. 2013). Of these, 43% have available Age_{JX} estimates. The spatial distribution of the MPCMs is associated with four isothermal cluster ellipses (Kuhn et al. 2014): the small (core radius 0.01 pc) subcluster A containing the embedded cluster around the BN-KL hot core, subcluster B representing the small and dense Trapezium core of the ONC cluster, the rich subcluster C containing both the ONC cluster and OMC cloud members, and subcluster D extending north-south along the OMC 1 filament behind the ONC.

Due to the unfavorable viewing angle where the ONC is superposed on the molecular cores, both the Kuhn et al. MPCM sample and the subset used here for Age_{JX} analysis for the subclusters A and D are significantly contaminated by the foreground ONC stars. A similar problem is evident in the X-ray study of the OMC 1 cores by Grosso et al. (2005). Our inferred low absorption and relatively high age for these embedded subclusters are likely not realistic. Meanwhile, the subcluster C is likely contaminated by the OMC objects.

The sophisticated analysis of optical data by Da Rio et al. (2010) for the ONC led to an age estimate of $2-3$ Myr. Further, combined with the *Hubble Space Telescope* photometry, these optical data of stars in ONC give an average age of 2.2 Myr (Reggiani et al. 2011). The optical data have good coverage of the outskirts of the ONC cluster extending beyond

the *Chandra* field but, due to the issues of absorption and high nebular emission, their sample misses many stellar members of the dense Trapezium region and the OMC 1 cloud cores.

The reliable Age_{JX} result for this region is that the inner Trapezium region appears young at 1.1 Myr and the 'unclustered' component appears older at 2.0 Myr (Figure 7). The apparent age gradient from the interior of the ONC to its outer region is discussed further in our companion paper (Getman et al. 2014) where we do a better job of separating between ONC and OMC members.

7.2. Flame Nebula

The Flame Nebula is a nearby ($D \sim 414$ pc) H II region in the Orion B cloud associated with the rich, obscured stellar cluster NGC 2024. Meyer et al. (2008) gives a detailed description of the region. There are over 480 MPCMs in the region (Broos et al. 2013) of which 21% have Age_{JX} estimates. The spatial distribution of the MPCMs is associated with the single elliptical isothermal cluster elongated along the direction of the molecular filament (Kuhn et al. 2014). The high median $J - H$ color for all MPCMs in the main cluster of 1.8 mag (equivalent to $A_V \sim 11$ mag) suggests that many cluster members are still embedded in the molecular filament.

The previously published age estimates of $\lesssim 0.3 - 0.5 - 1$ Myr, based on IR spectroscopy and photometry data (Levine et al. 2006, and references therein), indicate that the NGC 2024 cluster is very young. Our Age_{JX} analysis gives a median age of 0.8 Myr for the entire cluster, consistent with the previous estimates (Figure 8). The age of the less absorbed stellar population that is spatially distributed outside the molecular filament, in the outskirts of the *Chandra* field of view, is older around ~ 1.3 Myr. However, we have

also found a strong age gradient within the cluster such that the core is significantly older than the intermediate and outer regions. This is presented and discussed in the companion paper (Getman et al. 2014).

7.3. W 40

The W 40 is a nearby ($D \sim 500$ pc) blister H II region at the edge of the dense molecular core DoH 279-P7, which in turn is part of the Aquila Rift molecular cloud complex. A description of the region is given by Kuhn et al. (2010). There are over 420 MPCMs in the region (Broos et al. 2013); 21% have available Age_{JX} estimates. The spatial distribution of the MPCMs is modeled as a single rich isothermal sphere with core radius 0.15 pc (Kuhn et al. 2014). The high median $(J-H)$ color of 1.9 mag ($A_V \sim 11$ mag) is attributable to absorption both in the cloud screen and local molecular material.

Age_{JX} results are shown in Figure 8 and listed in Table 2. The $Age_{JX} \sim 0.8$ Myr for the cluster supports the very young age $\lesssim 1$ Myr inferred from the high fraction of K-band excess stars (Kuhn et al. 2010). A strong spatial gradient in age from the young cluster to an older unclustered component (~ 1.5 Myr) is seen.

7.4. RCW 36

RCW 36 is a nearby ($D \sim 700$ pc) H II region associated with one of the numerous molecular clumps of the giant molecular filament Vela-C (Pettersson 2008; Ellerbroek et al. 2013). There are over 380 MPCMs in the region (Broos et al. 2013); 22% have Age_{JX} estimates. According to Kuhn et al. (2014) the spatial distribution of the MPCMs is characterized by a core-halo cluster structure with the core (halo) ellipses elongated perpendicular (parallel) to the molecular filament. We find here that the stars in the cluster

core have a redder median $J - H$ color of 2.2 mag ($A_V \sim 14$ mag) than the stars in the cluster halo ($J - H = 1.7$ mag, $A_V \sim 10$ mag), suggesting that the core is more embedded in the cloud.

There are insufficient number of 2MASS-JHK_s stars with reliable photometry for Age_{JX} analysis of the cluster core (B). The inferred age of the cluster halo (A) is 0.9 Myr, and the dispersed unclustered stars are older with $Age_{JX} \sim 1.9$ Myr. From a spectroscopic study of several dozen members, Ellerbroek et al. (2013) find the most common age of members is around 1.1 Myr with a tail to several Myr. They do not find a spatial gradient in ages, but their sample generally lies within the core radius of our component A, omitting many dispersed stars in our unclustered component.

7.5. NGC 2264

NGC 2264 ($D \sim 913$ pc) is a composite star forming region with both embedded and revealed clustered components and a filamentary molecular structure within the Mon OB1 molecular cloud complex (Dahm 2008; Feigelson et al. 2013). There are nearly 1200 MPCMs in the region (Broos et al. 2013); 25% have Age_{JX} estimates. The spatial mixture model of Kuhn et al. (2014) has 13 subclusters: seven in the lightly absorbed northern region (A, B, C, D, and H around the Fox Fur Nebula; E and F near/around the O-type binary S Mon), and six in the mostly embedded southern region (G, I, and J projected against the molecular core in the IRS 1 region; K, L, and M in the IRS 2 region).

The stellar population of NGC 2264 has been studied for decades. Recent published age estimates for the stars in the complex, mainly based on optical data, range from 1.5 to 3 Myr (Dahm et al. 2007; Mayne et al. 2007; Baxter et al. 2009). The Age_{JX} estimates are generally similar. Our principal new result is an age gradient between the richest northern

subclusters (D and E; $Age_{JX} \sim 3.2$ Myr) and the southern subclusters (G, I, J, and M; ~ 1.5 Myr). This is consistent with the *Herschel* satellite image of the cold dust where the northern subclusters are associated with more dispersed molecular material. Both the rich southern subcluster K ($Age_{JX} \sim 2.2$ Myr) and the dispersed stars in the region ($Age_{JX} \sim 2.8$ Myr) exhibit intermediate ages.

7.6. Rosette Nebula

The Rosette Nebula ($D \sim 1.33$ kpc) is an H II bubble region ionized by the unobscured rich cluster NGC 2244. Star formation in the region has been extensively studied (Román-Zúñiga & Lada 2008; Wang et al. 2010; Ybarra et al. 2013). The *Chandra* mosaic encloses NGC 2244 and an extended portion of the filamentary Rosette Molecular Cloud (RMC) to the southeast. There are over 1700 MPCMs in the region (Broos et al. 2013); 19% have available Age_{JX} estimates. The spatial analysis of Kuhn et al. (2014) identified 15 subclusters: 8 northwestern subclusters inside the ionized bubble (A, B, C, D, E, F, G, and H associated with the NGC 2244 and NGC 2237 clusters), 3 subclusters at the northwestern end of the molecular cloud (I, J, and K), and 4 subclusters that lie projected against the densest parts of the southeastern cloud (L, M, N, and O). As expected, we find that the clusters inside the bubble are much less absorbed with median $(J-H) \sim 0.6-0.8$ mag (or $A_V \lesssim 1.5$ mag) than the clusters associated with cloud cores with median $(J-H) \sim 1-2$ mag (or $A_V \sim 4-15$ mag).

Ybarra et al. (2013) estimates ages of $\sim 2-3$ Myr for NGC 2244 and ~ 1 Myr for the stars in the cloud clusters based on their infrared disk fractions. Our Age_{JX} values are consistent with these estimates. The main result of our analysis is that we detect an age gradient: the distributed stellar population and the sparse subclusters B, C, F on the periphery of NGC 2244 have ages $\gtrsim 4$ Myr; NGC 2244 itself (E) has age ~ 3 Myr; and

the molecular cloud subclusters (J, M, N, and O) have ages $\sim 1-2$ Myr. Notice that for subclusters M and O, the Age_{JH} values are preferred over the Age_{JX} estimates due to the poor sensitivity of the Age_{JX} sample to heavily embedded members. We also find that the rich cluster L is superposed in front of the Rosette Molecular Cloud with less absorbed stars and an older ($\gtrsim 2.7$ Myr) inferred age.

7.7. Lagoon Nebula

The Lagoon Nebula ($D \sim 1.3$ kpc) is defined by a large H II bubble ionized by the cluster NGC 6530. The *Chandra* field encloses the southern portion of the bubble with the main cluster, a complex interface between the bubble and molecular cloud with numerous bright-rimmed components, and the bright Hourglass Nebula region to the west of the main cluster. Descriptions of the star forming complex are given by Tothill et al. (2008) and Kumar & Anandarao (2010). The region is very rich in X-ray sources with over 2000 MPCM stars (Broos et al. 2013); 31% have Age_{JX} estimates. The spatial analysis of Kuhn et al. (2014) identified 11 subclusters: three associated with the Hourglass region (B, C, and D), seven associated with NGC 6530 (E, F, G, H, I, J, and K), and one to the northwest of the Hourglass (A). Except for the B and K with median $(J-H) \sim 1.1$ mag ($A_V \sim 4$ mag), all are lightly absorbed with $(J-H) \sim 0.8-0.9$ mag ($A_V < 3$ mag).

The age analysis of Prisinzano et al. (2012) based on optical data indicated a younger < 2 Myr stellar population in the southeastern portion of the field and an older (> 2 Myr) stellar populations in the northern and southwestern parts of the field. Our age results are somewhat different. We find younger ($\lesssim 2$ Myr) star concentrations in clusters projected against the molecular cloud including the K subcluster near the M8 E cloud, E subcluster near the South Eastern Bright Rim cloud, and B and C subclusters near the HW clump (these molecular structures are shown in Tothill et al. 2008). The subclusters north of the

cloud (A, F, I, and J) and G and H subclusters near the Central Ridge clump are found to be older with ages $2.0 - 2.6$ Myr. The large-scale unclustered component has median age of 2.2 Myr.

7.8. NGC 2362

With no molecular material left in its immediate vicinity, the NGC 2362 cluster ($D \sim 1.48$ kpc) is perhaps the oldest MYStIX target. There are nearly 500 MPCMs (Broos et al. 2013) of which 24% have Age_{JX} estimates. For detailed description of the region see Dahm (2008b). The spatial analysis of Kuhn et al. (2014) identifies two subclusters; the principal cluster B harbors the most massive star τ CMa and most of the cluster members; and the small subcluster A represents a concentration of stars to the north. Both components exhibit low absorption, $(J - H) \simeq 0.6$ mag (or $A_V \lesssim 1$ mag).

The previous age estimate based on optical data is $\sim 3.5 - 5$ Myr (Dahm 2005). We find a large-scale age gradient: the stars in the primary cluster are significantly younger (~ 2.9 Myr) than the stars of the distributed population (~ 3.8 Myr). There is also a systematic difference between the Dahm et al. ages and those derived here, which is entirely due to different choice of pre-main sequence evolutionary models, Baraffe et al. (1998) in place of Siess et al. (2000).

7.9. DR 21

DR 21 ($D \sim 1.5$ kpc) is a star forming region associated with a long and dense molecular filament in the giant Cygnus X star forming complex (Kumar et al. 2007; Reipurth & Schneider 2008). There are nearly 1000 MPCMs, both embedded in the DR 21 filament and distributed within the Cygnus-X complex; 14% have Age_{JX} estimates. The

spatial analysis of Kuhn et al. (2014) identifies nine clusters, all positioned and elongated along the molecular filament. With median $J - H \simeq 2 - 3$ mag (corresponding to $A_V \simeq 13 - 22$ mag), these are among the most heavily absorbed MYStIX structures.

Kumar et al. (2007) find an age of ~ 3 Myr for the NIR stellar population in the region, but suggest a younger age of $\lesssim 1$ Myr for the clustered mid-infrared population. The results of our age analysis are consistent with these values. We find a strong age difference between the older ~ 2.5 Myr unclustered stellar population uniformly distributed outside the molecular filament, and the younger $\lesssim 1$ Myr stellar population grouped in the small clusters embedded in the molecular cores along the filament. Age_{JX} estimates are not available for some of the heavily embedded clusters (B, C, G, and H), but the alternative Age_{JH} estimates indicate that these are all very young ($\lesssim 1$ Myr). The age gradient may be due either to the dispersion of older stars from the DR 21 clouds, or to an age difference between the embedded DR 21 stellar population and the large-scale Cygnus X population of pre-main sequence stars arising from many past star forming regions in the complex.

7.10. NGC 6334

NGC 6334 ($D \sim 1.7$ kpc) is a massive star forming region associated with a long and dense molecular filament part of a larger cloud that also produced the NGC 6357 complex (Persi & Tapia 2008; Feigelson et al. 2009; Russeil et al. 2010). The MYStIX field has nearly 1700 MPCMs (Broos et al. 2013), but only 7% have Age_{JX} estimates due to the shallow X-ray data that inhibit derivation of reliable stellar L_X estimates. The spatial analysis of Kuhn et al. (2014) identifies 14 stellar structures: six clusters lie projected against the molecular filament (D, E, J, K, L, and M), one subcluster is associated with a molecular patch northeast of the main filament (N), and seven clusters lie superposed around the filament (A, B, C, F, G, H, and I). This last group has lower obscuration,

$(J-H) \simeq 1.0-1.6$ mag ($A_V \simeq 3-9$ mag), than the clusters embedded in the densest parts of the filament (J, K, L, and N) with $(J-H) \simeq 1.9-3.0$ mag ($A_V \simeq 12-22$ mag).

Persi & Tapia (2008) assume an age of $\lesssim 1$ Myr. Our Age_{JX} analysis gives an age ~ 1.1 Myr for the combined heavily absorbed subclusters L and J, significantly younger than the dispersed stellar population with median age ~ 1.9 Myr. The alternative Age_{JH} procedure indicates that the heavily absorbed subclusters D, E, K, L, and N are very young with ages $0.6-0.9$ Myr. The remaining subclusters have insufficient information for age analysis.

7.11. NGC 6357

NGC 6357 ($D \sim 1.7$ kpc) is a massive star forming region divided into three major cluster complexes that are associated with the three H II bubbles, CS 59, CS 61, and CS 63 (Wang et al. 2007; Russeil et al. 2010; Fang et al. 2012). The stellar population is rich with over 2200 MPCMs (Broos et al. 2013); 13% have available Age_{JX} estimates. The spatial analysis of Kuhn et al. (2014) identifies 6 subclusters: A, associated with the rich Pismis 24 cluster, and B lie in the CS 61 bubble; C, D, and E in the CS 63 bubble; and F in the CS 59 bubble. All subclusters are subject to similar absorption with median $J-H \simeq 1.3-1.4$ mag ($A_V \simeq 6-7$ mag).

Based on analysis of optical properties of Pismis 24, Fang et al. (2012) find an age of 1 Myr. Our Age_{JX} value for subcluster A is close at 1.4 Myr. We find no promising age gradients in the full MYStIX region. Despite the diverse morphology of the stellar and the molecular components in the region, most of the MYStIX stars, both in the clusters and those uniformly distributed across the bubbles and the bubble edges, have similar ages of $1.0-1.5$ Myr. It seems that the star formation proceeded nearly simultaneously across this

region.

7.12. Eagle Nebula

The Eagle Nebula ($D \sim 1.75$ kpc) is an H II region ionized by the rich cluster NGC 6611. The giant molecular cloud surrounding the cluster is composed of numerous dense molecular clumps and bright-rimmed components including the famous Pillars of Creation, Spire Pillar, and Bright Rimmed Cloud 30 (Indebetouw et al. 2007; Oliveira 2008; Hill et al. 2012). The MYStIX region has over 2500 MPCM stars (Broos et al. 2013) of which 19% have Age_{JX} estimates. The spatial analysis of Kuhn et al. (2014) identifies twelve subclusters: three associated with the NGC 6611 cluster (A, B, and C); two possibly associated with the Spire Pillar (D and K); four related to the M16-N cloud (E, G, H, and I); two at the northern edge of the *Chandra* field with no obvious cloud associations (J and F); and one at the southeastern edge of the field projected against the M16-E cloud (L). The NGC 6611 components have the lowest obscuration with $(J-H) \lesssim 1.0$ mag ($A_V \lesssim 3$ mag), while the small clusters associated with dense molecular patches (E, G, H, I, and L) are subject to the highest absorption with $(J-H) \sim 1.6-2.6$ mag ($A_V \simeq 9-18$ mag). The remaining subclusters (D, K, J, and F) are subject to the intermediate absorption.

Based on optical and IR data, Guarcello et al. (2010b) report an age gradient in Eagle Nebula: with the youngest stars toward the north ($\sim 0.3-0.8$ Myr), intermediate-age stars in the NGC 6611 cluster ($0.8-1.3$ Myr), and the oldest stars to the southeast (~ 2.6 Myr). The result of our age analysis qualitatively agrees with these findings: we find the northern structures E, G, H, and I associated with cores of the M16-N cloud to be much younger ($\simeq 0.7-1.3$ Myr) than the stars in the subclusters A, B, C, and D that compose the principal ionizing cluster NGC 6611 ($\simeq 1.5-2.5$ Myr). However, our individual inferred age values for these cluster structures are systematically older than those

found by Guarcello et al. We obtain different results in the southeast region. Instead of the oldest stars, we find intermediate-age compact subcluster K near the base of the molecular Spire pillar ($Age_{JX} \sim 1.9$ Myr) and very young subcluster L near a core in the M16-E cloud ($Age_{JH} \sim 1.0$ Myr).

7.13. M 17

M 17 ($D \sim 2.0$ kpc), one of the brightest H II regions in the sky, is ionized by the massive cluster NGC 6618. The H II region lies at the southwestern edge of the enormous extended bubble M17 EB, and it interacts energetically with the surrounding giant molecular cloud producing photodissociation regions at the edges of the two massive cloud components, M17 SW and M17 North (Broos et al. 2007; Chini & Hoffmeister 2008; Povich et al. 2009). There are nearly 2400 MPCMs in the MYStIX field (Broos et al. 2013); 21% have Age_{JX} estimates. The spatial analysis of Kuhn et al. (2014) identifies fifteen subclusters: three associated with dense portions of the M17 SW cloud (A, B, and F); three projected against the edge of the M17 SW cloud (C, G, and H); one near the edge of the M17 North cloud (M); and eight constituting parts of the rich but clumpy NGC 6618 cluster (D, E, I, J, K, L, N, and O). Most of the structures that lie projected against cloud components are highly absorbed (A, B, C, F, and M have median $(J-H) \simeq 1.7-2.5$ mag or $A_V \simeq 10-17$ mag), whereas most of the structures associated with NGC 6618 are less absorbed ($(J-H) \simeq 1.3-1.5$ mag or $A_V \simeq 6-8$ mag). Note that Kuhn et al. performed the cluster analysis using only the *Chandra* exposure centered on NGC 6618 (Figure 19), while the Age_{JX} analysis here also treats outer *Chandra* exposures (Figure 20). We consider these stars to be unclustered.

Based on optical and IR data, Hoffmeister et al. (2008) estimate an age of ~ 0.5 Myr for the youngest generation of stars in the region. We find homogeneous subcluster ages

within the NGC 6618 and M17 SW regions at $Age_{JX} \simeq 1 - 1.4$ Myr. We find older ($\sim$ 3 Myr) stars in the eastern *Chandra* field that covers part of the extended bubble M17 EB, and intermediate-age stars that lie projected in between NGC 6618 and M17 EB with $Age_{JX} \sim 1.7$ Myr. A large-scale east-west age gradient is thus present in this region but no evident small-scale temporal structure. Within the M17 SW cloud, our Age_{JX} analysis is likely not sensitive to the embedded population associated with the UC1 and Kleinman-Wright Object ultra-compact H II regions, but instead samples an older ($\sim$ 1.4 Myr) less absorbed and distributed sub-population. Our alternative Age_{JH} analysis indicates a younger age of $\lesssim 1$ Myr for the subclusters in the cloud (A, B, C, F, and M).

7.14. Carina Nebula

The Carina Nebula is one of the richest star-forming complexes in the Galaxy's spiral arms, a starburst 'cluster of clusters' with star formation over an extended time and region. It was extensively studied at X-ray and infrared wavebands in the *Chandra Carina Complex Project* (Townsley et al. 2011). The region harbors a chain of very rich stellar clusters − Tr 15, Tr 14, and Tr 16 from north to south −, several secondary clusters, and active star formation in the South Pillars region. Tr 15 appears to be oldest, missing its massive O stars (earlier than O9) probably to supernova explosions (Wang et al. 2011). Tr 16 is also old with post-main sequence massive stars including the famous luminous blue variable η Car which is expected to go supernova soon. Tr 14, on the other hand, lies near a dense molecular cloud and appears to be significantly younger. There are over 7300 MPCMs in the MYStIX study region (Broos et al. 2013); 16% have Age_{JX} estimates.

The spatial analysis of Kuhn et al. (2014) identifies twenty subclusters: three subclusters associated with Tr 15 (I, H, and F); three associated with Tr 14 (A, B, and C); one for Collinder 232 (D); four associated with Tr 16 (E, J, K, and L); and the remaining

sub-clusters (M, N, O, P, Q, R, S, and T) associated with the South Pillars. The very elongated ellipse G covers heterogeneous structures in the Carina Complex and should not be viewed as a distinct structure. Most of the structures are lightly absorbed with medians $(J-H) \simeq 0.8-1.0$ mag ($A_V \simeq 1-3$ mag). The principal exception is embedded Treasure Chest cluster (O) with $(J-H) \simeq 1.2$ mag ($A_V \gtrsim 5$ mag).

Based on near-IR data, Preibisch et al. (2011) give age estimates of (from north to south) $5-8$ Myr for Tr 15, $\lesssim 3$ Myr for Tr 14 and Collinder 232, $3-4$ Myr for Tr 16, and < 1 Myr for the Treasure Chest. For the major Trumpler clusters, our Age_{JX} estimates show similar results when averaged over the rich clusters, although our ages are systematically younger. But we find heterogeneity in structure and age within these rich clusters. In Tr 15, the central cluster H with the massive stars has age ~ 2.8 Myr while the remaining two secondary subclusters, I and F, and the stellar population in the outskirts of the region are substantially older ($\gtrsim 4.5$ Myr). Tr 14 is youngest but with a younger core component at 1.5 Myr and an older halo component at 2.7 Myr; this result is qualitatively consistent with the core-halo age gradient reported by Ascenso et al. (2007). The Tr 16 region is diverse. The subcluster K harboring η Car is oldest at 3.6 ± 0.7 Myr, consistent with the theoretical minimum age of ~ 3 Myr for the supergiant η Car (Smith & Brooks 2008). The remaining cluster structures in Tr 16 are younger (~ 2.5 Myr) and lie projected closer to the denser parts of the molecular cloud.

The South Pillars region harbors stellar populations of different ages with a wide range of ages from 1 to 5 Myr. Some portions of the South Pillars region show a bimodal age distribution suggesting superposed younger and older populations. This supports the scenario presented by Povich et al. (2011) and Feigelson et al. (2011) that these clouds have been (and will continue to) produce stars over an extended period of triggered star formation. The Treasure Chest is the only localized distinct cluster that is young with

$Age_{JX} \simeq 1.1$ Myr.

7.15. NGC 1893

The most distant MYStIX target, NGC 1893 at $D \simeq 3.6$ kpc, is a giant H II region surrounded by $\sim 1.5^\circ$ diameter incomplete ring of molecular cloud. The MYStIX field encompasses the central part of the region where most cloud material has been evacuated (Caramazza et al. 2008; Prisinzano et al. 2011; Pandey et al. 2013). There are about 1300 MPCMs (Broos et al. 2013); 27% have Age_{JX} estimates by virtue of an unusually long *Chandra* exposure. The spatial analysis of Kuhn et al. (2014) divides the central cluster into a linear chain of ten subclusters. The subclusters G and J are located at the heads of giant molecular pillars and exhibit mild absorption with $(J-H) \simeq 1.0$ mag ($A_V \simeq 3$ mag). All the other subclusters are lightly absorbed with $A_V \simeq 1$ mag.

According to the optical analyses of Prisinzano et al. (2011) and Pandey et al. (2013), the majority of young stars in the region have ages between $\lesssim 1$ and 5 Myr with median age around 1.5 Myr. Our age analysis shows that the distributed stellar population is older, with median $Age_{JX} \simeq 3$ Myr, than the majority of the clustered population. A dramatic spatial gradient in subcluster ages is seen with the older structures ($2.6 - 3.5$ Myr; A, B, and C) lying at the southwestern end of the cluster chain and the younger subclusters ($1.4 - 2.1$ Myr; D, F, G, H, and J) lying at the northeastern end of the chain. The northeastern structure I is an exception from this gradient; however, the age histogram for its constitute stars appears bimodal suggesting superposition of younger and older stellar populations.

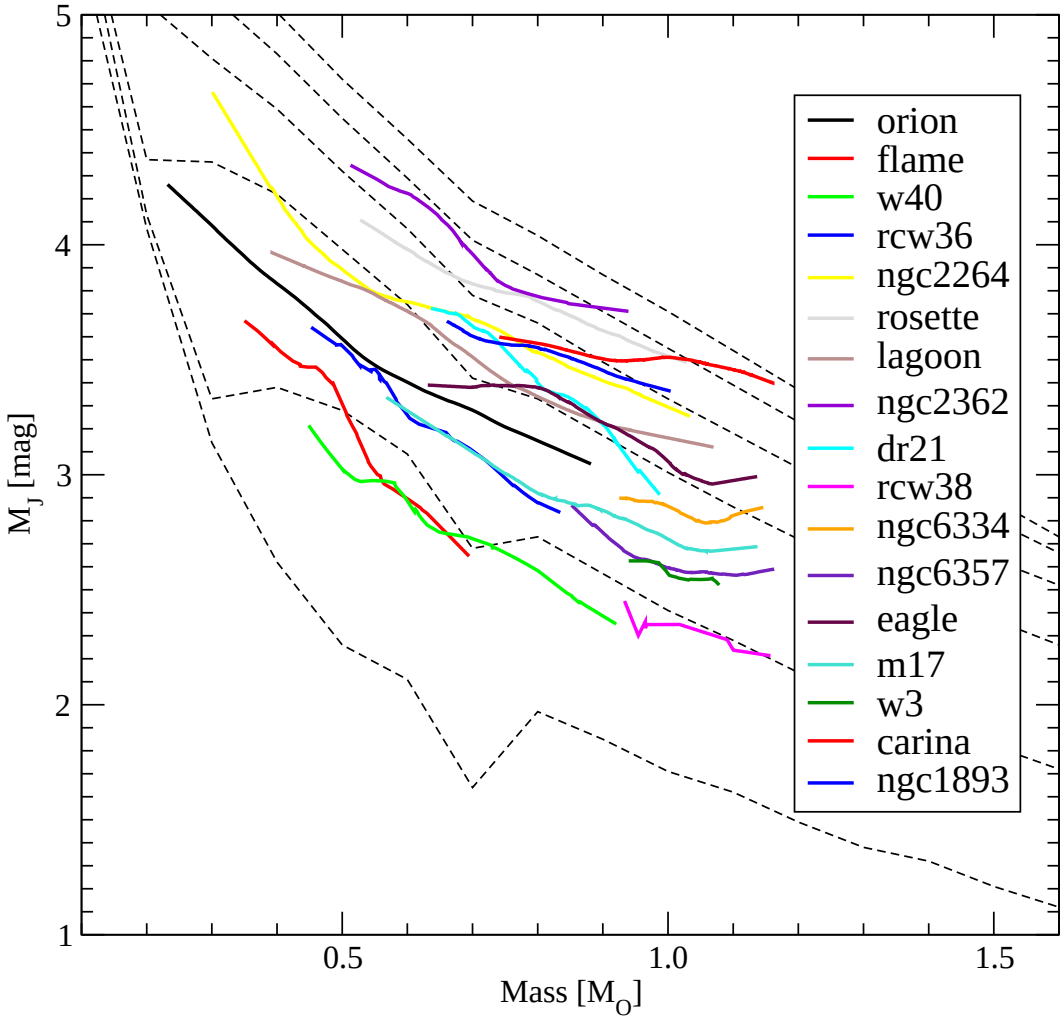

Fig. 1.— Friedman's super smoother regression fits (Friedman 1984) derived for 17 MYStIX massive star forming regions from $\sim$ 5500 MYStIX Probable Complex Members (MPCM) in a diagram of absolute J-band magnitude *vs*. stellar mass. The dashed lines show, from bottom to top, 0.5, 1, 2, 3, 4 and 5 Myr PMS isochrones from Siess et al. (2000).

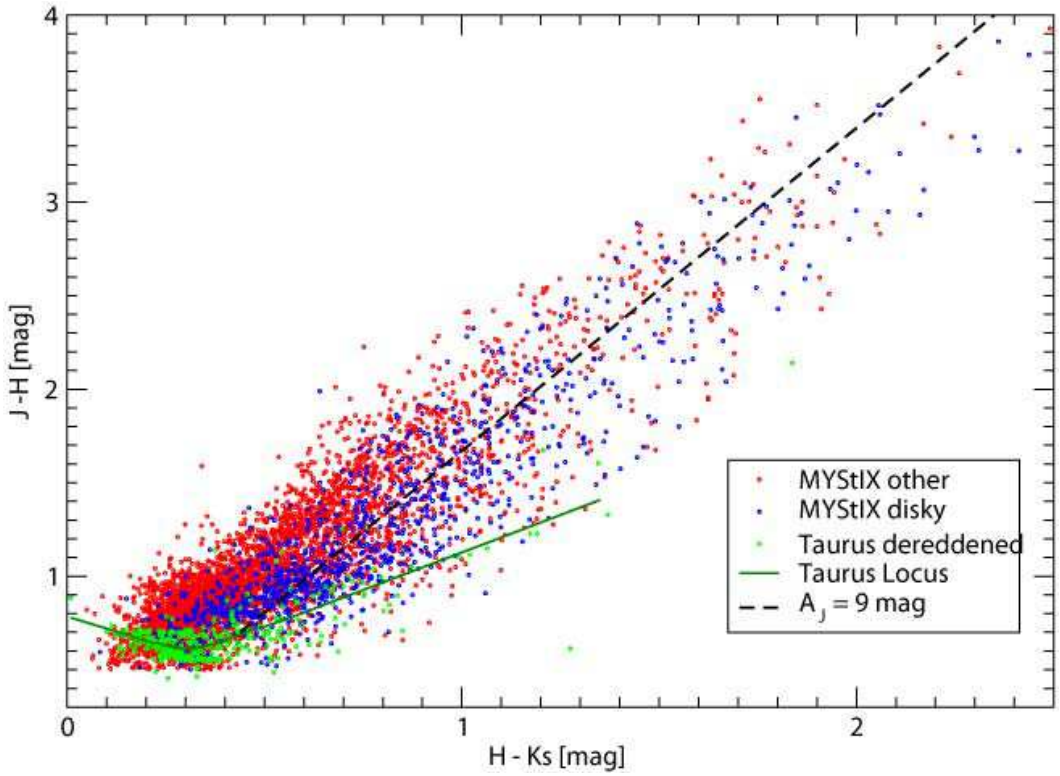

Fig. 2.— Near-IR color-color diagram for 5525 MYStIX young stars that are selected for the age analysis. Disk-bearing stars are in blue, and the remaining MYStIX stars are in red. The dereddened Taurus stars are marked by green points; Friedman's super smoother regression fit (Friedman 1984) to these data is shown by the green line. Dashed black line is a reddening vector of $A_J = 9$ mag originating at ~ 0.1 $M_\odot$(for the age of 1 Myr; Siess et al. 2000).

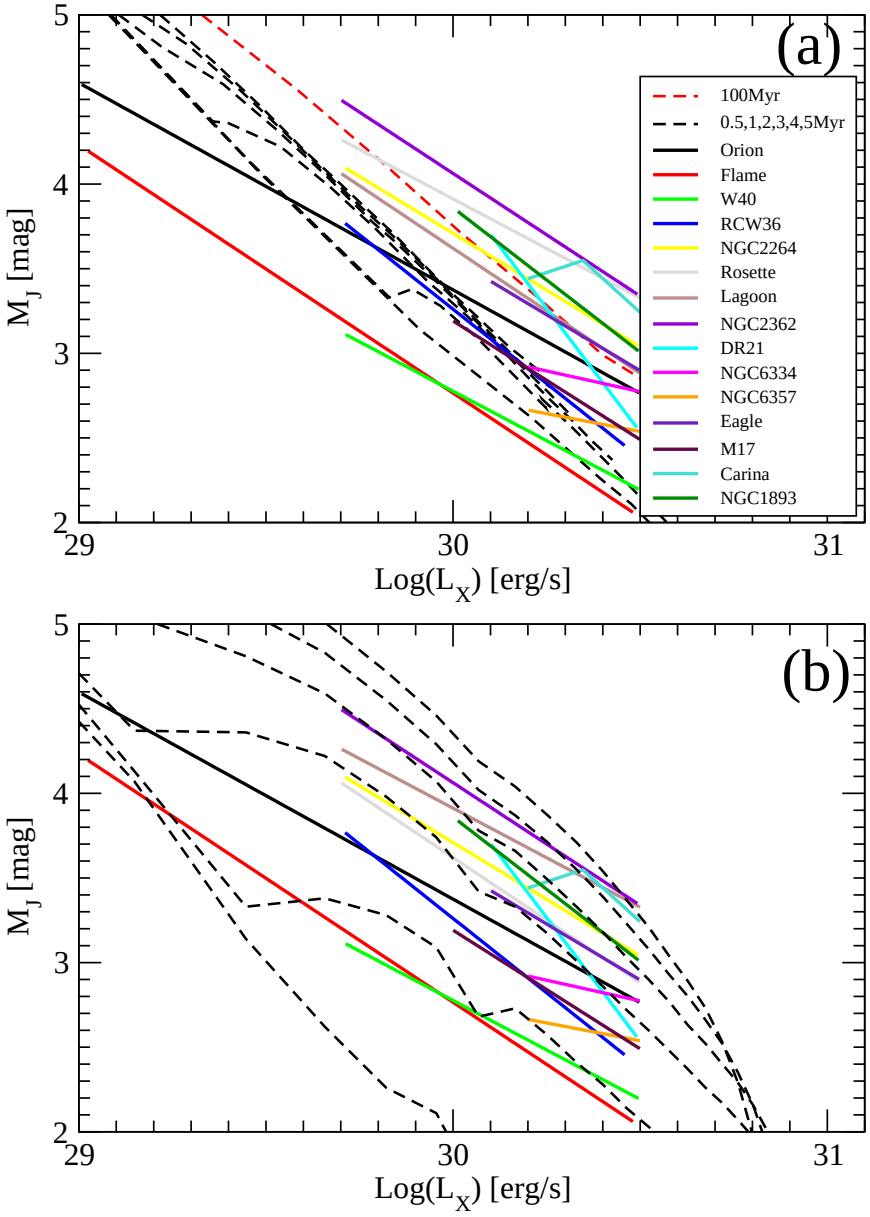

Fig. 3.— The MYStIX data in the form of the B-spline 50% quartile regression lines (colored solid lines; He & Ng 1999) are compared to the theoretical PMS isochrones of Siess et al. (2000) transformed onto $M_J - \log(L_X)$ plane, as described in the text (dashed lines). (a) The Seiss et al. isochrones are given for the two scenarios: (a) constant in time L_X/L_{bol} ratio, and (b) constant in time $L_X - M$ relation.

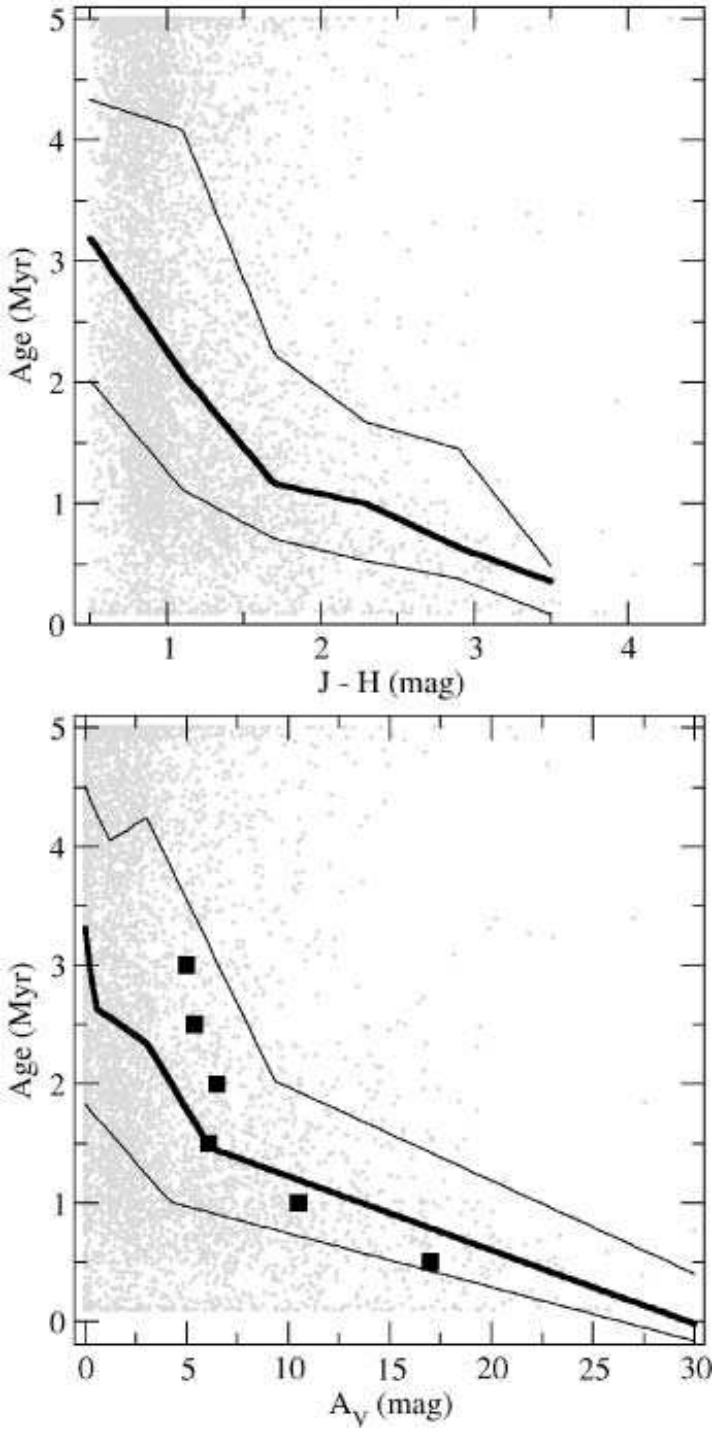

Fig. 4.— The relationship between Age_{JX} and absorption for 5525 MYStIX stars (grey ∘) where absorption is measured by (a) $J-H$ and (b) A_V. The black thick (thin) lines show the relationship of the median (25% and 75% quartiles) of Age_{JX} and absorption obtained from spline regression (see text for details). Values obtained by Ybarra et al. (2013) for Rosette region clusters are shown as black □.

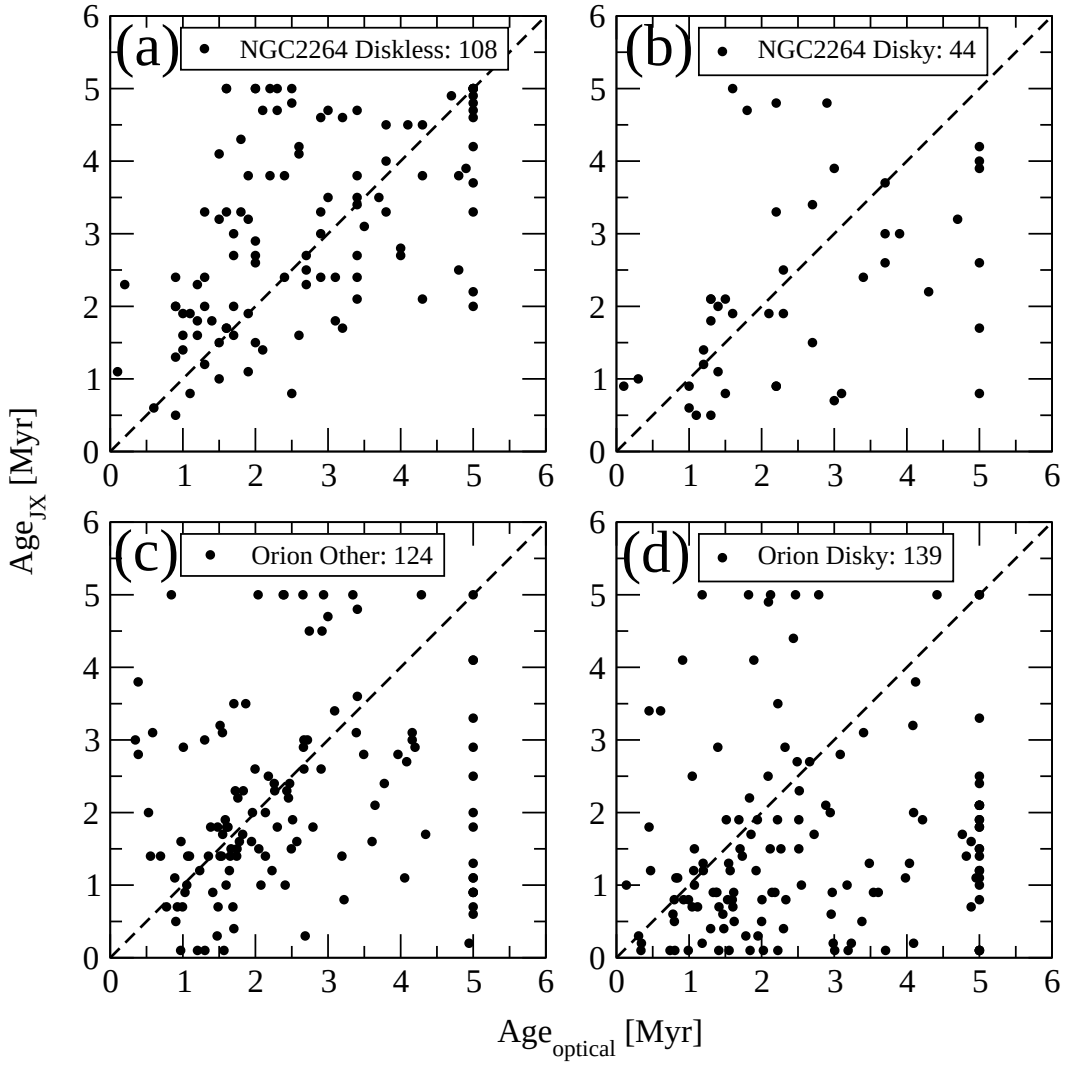

Fig. 5.— Comparison of stellar ages derived here from infrared and X-ray data (Age_{JX}) with ages derived from optical Hertzsprung-Russell or color magnitude diagrams Age_{opt}. Left panels show mainly disk-free stars and right panels show disk-bearing stars. Top panels show NGC 2264 stars and bottom panels show Orion Nebula stars. Black dashed lines indicate expected locus if the two methods give identical ages. Stars shown at 5 Myr (0.1 Myr) have inferred age estimates $\gtrsim$ 5 Myr ($\lesssim$ 0.1 Myr).

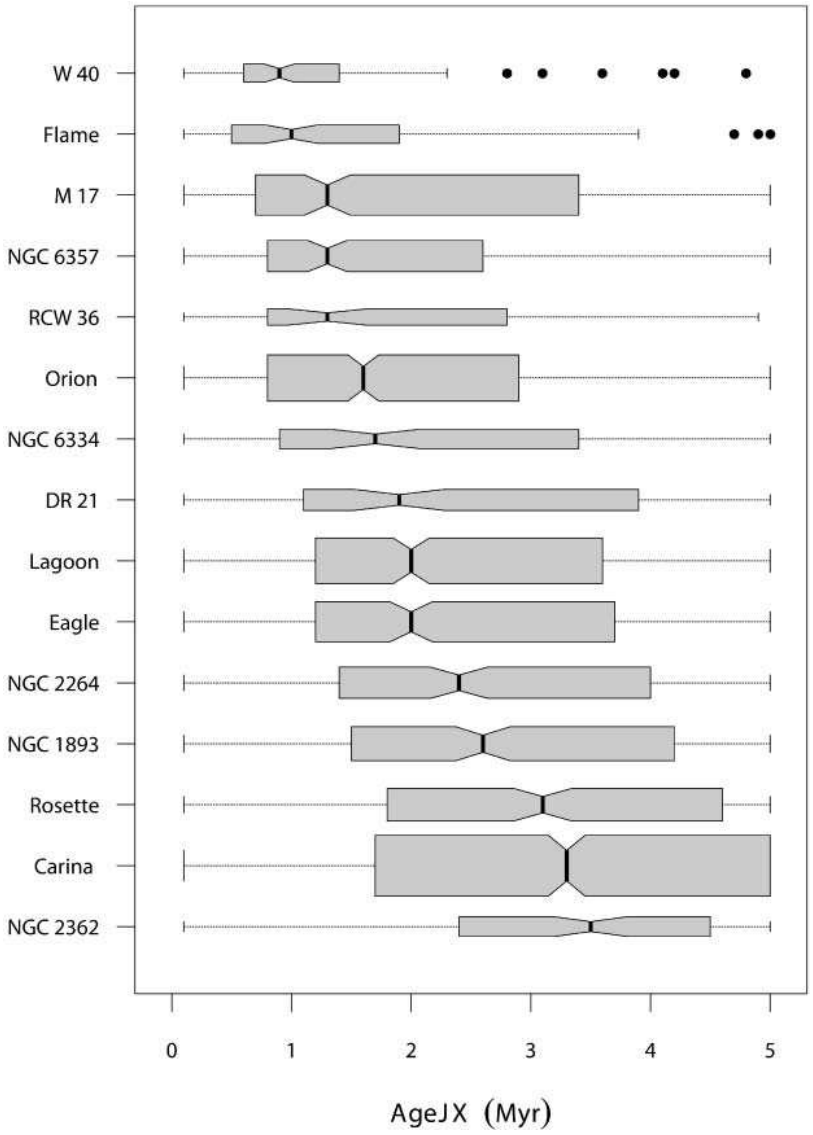

Fig. 6.— Boxplots of the Age_{JX} distributions for the MYStIX massive star forming regions shown in order of youngest (top) to oldest (bottom) median ages. The median age is shown as a dark bar. See text for details.

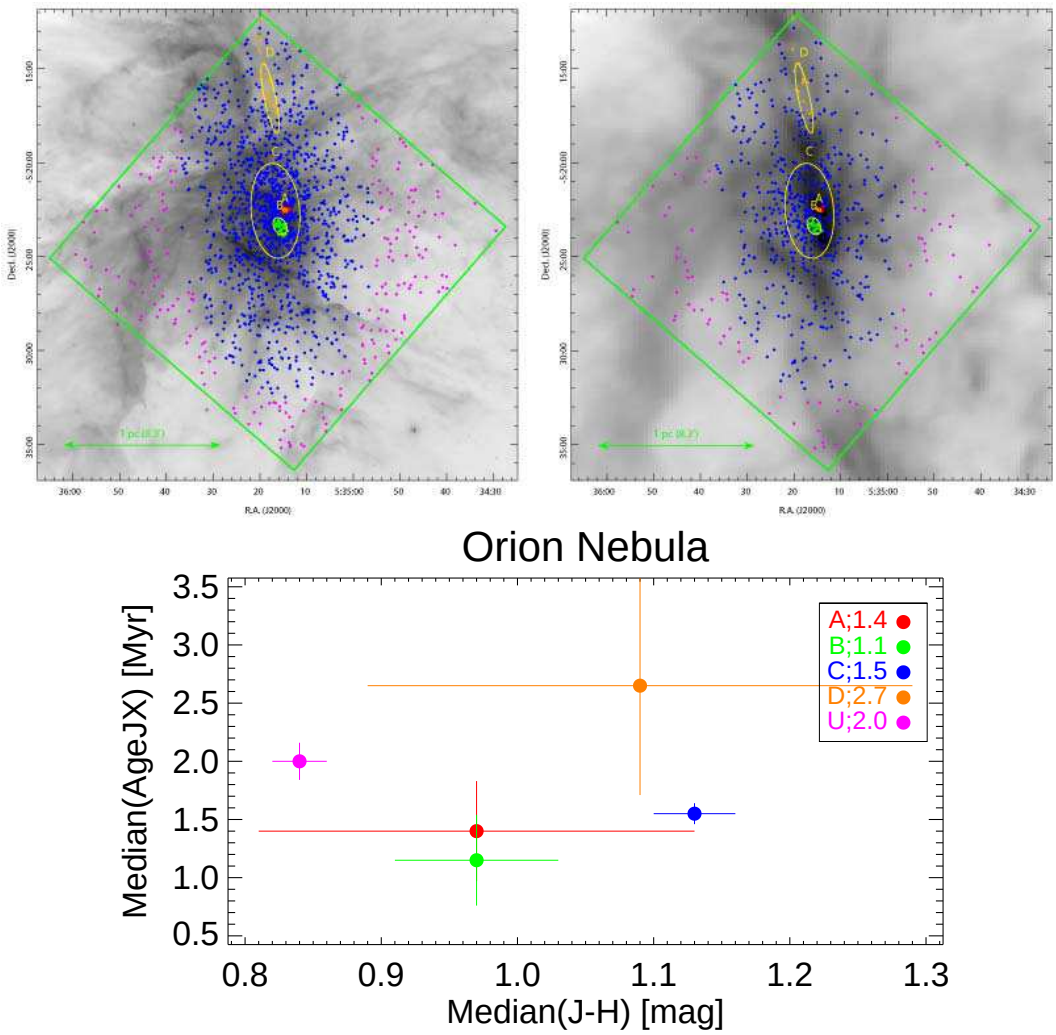

Fig. 7.— Age_{JX} analysis of the Orion Nebula. *Upper left:* The full MPCM sample with subcluster membership coded by color and the elliptical contours (yellow) showing the core radii of the isothermal structures from Kuhn et al. (2014). These symbols are superimposed on the 8.0 μm *Spitzer*-IRAC image. In this and following figures, the unclustered/ambiguous stars are shown in magenta color, and the *Chandra* field of view is outlined by the green polygon. *Upper right:* The subset of MPCM stars available for Age_{JX} analysis and the elliptical contours superposed on the 500 μm *Herschel*-SPIRE image. *Lower:* The median Age_{JX} estimates for the four subclusters and the unclustered component plotted against their respective median $(J-H)$ color indices. The legend identifies each point with a subcluster and states the median age in Myr. These ages are listed in Table 2.

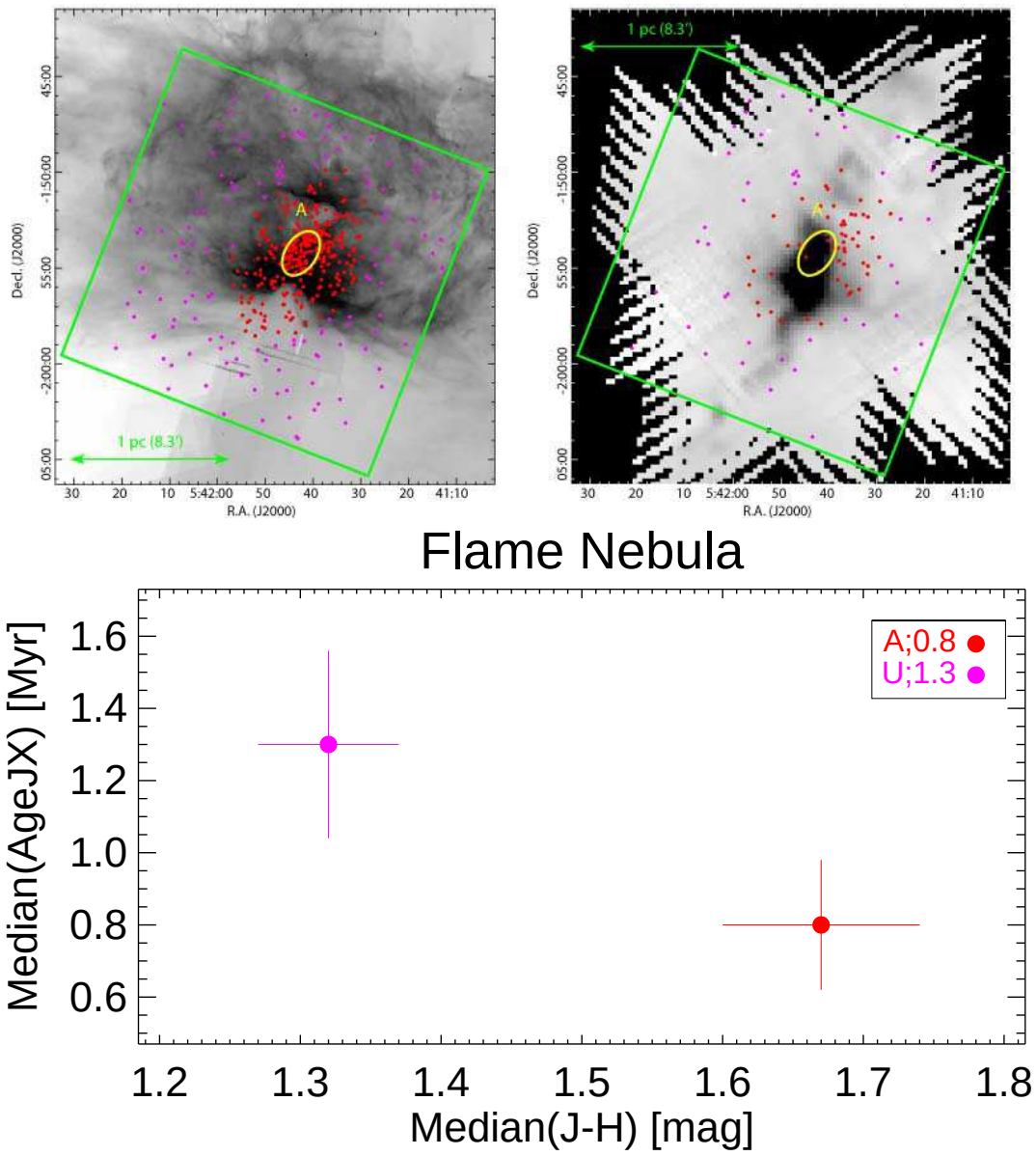

Fig. 8.— Age_{JX} analysis of Flame Nebula. See Figure 7 for description.

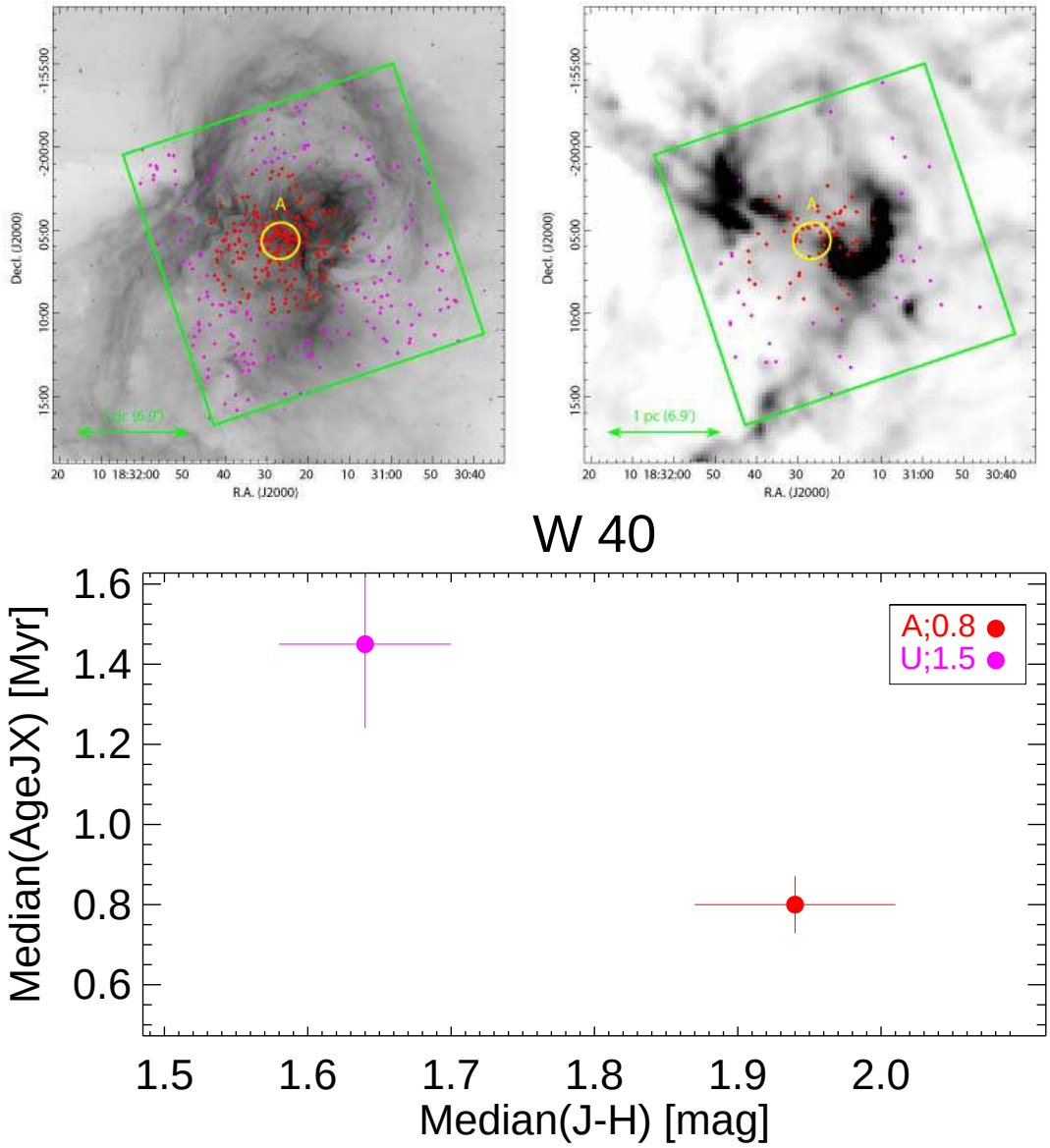

Fig. 9.— Age_{JX} analysis of W 40. See Figure 7 for description.

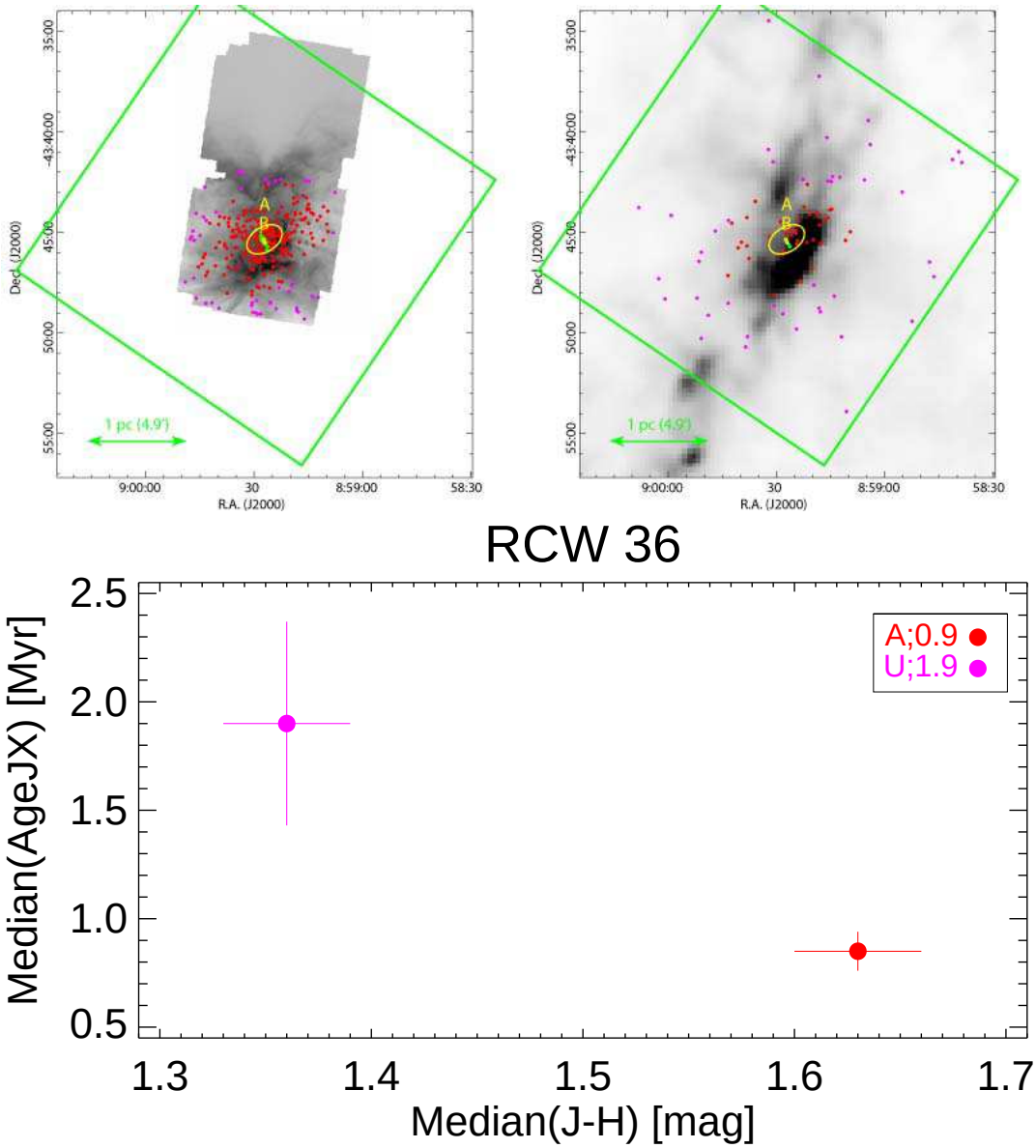

Fig. 10.— Age_{JX} analysis of RCW 36. See Figure 7 for description.

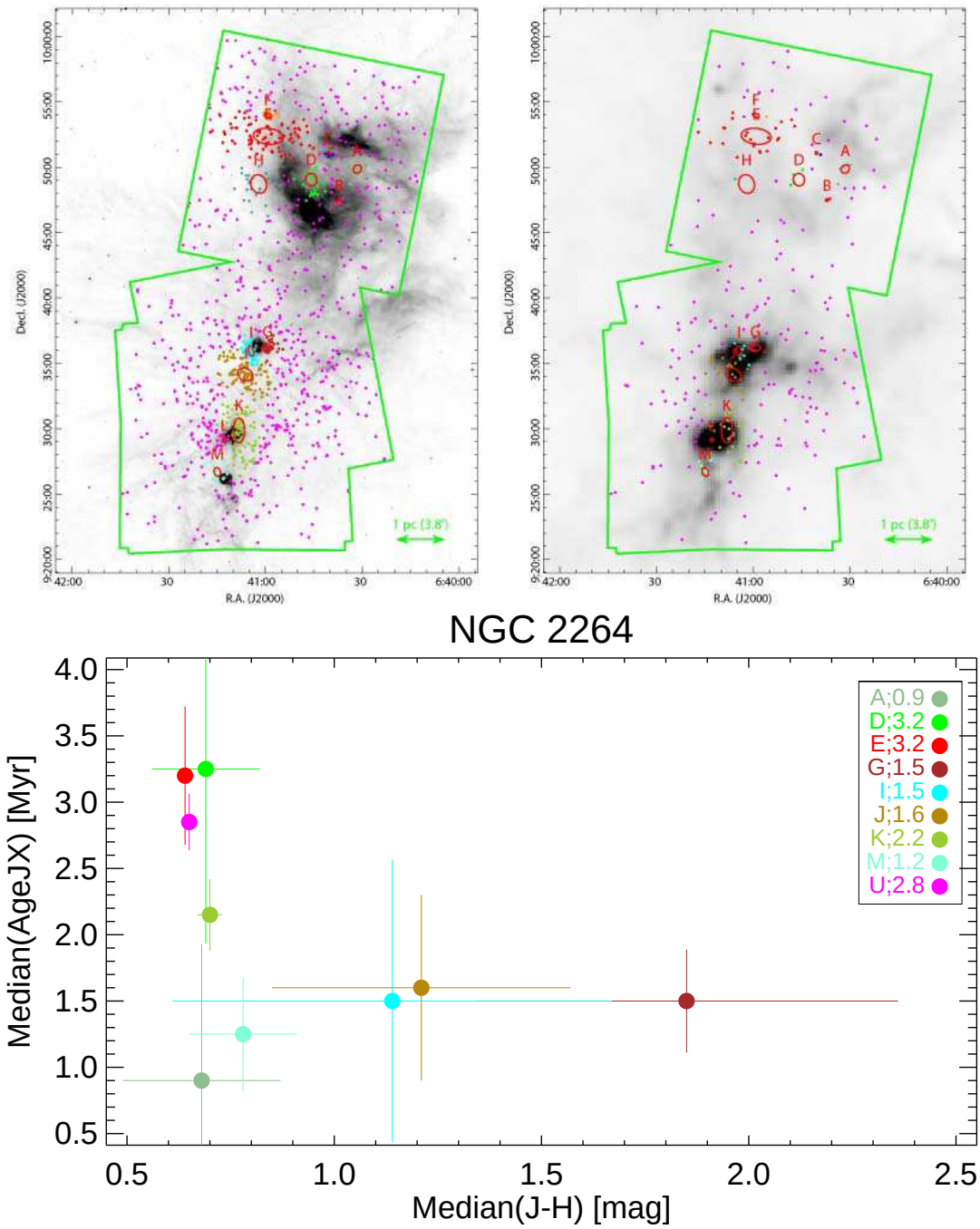

Fig. 11.— Age_{JX} analysis of NGC 2264. See Figure 7 for description.

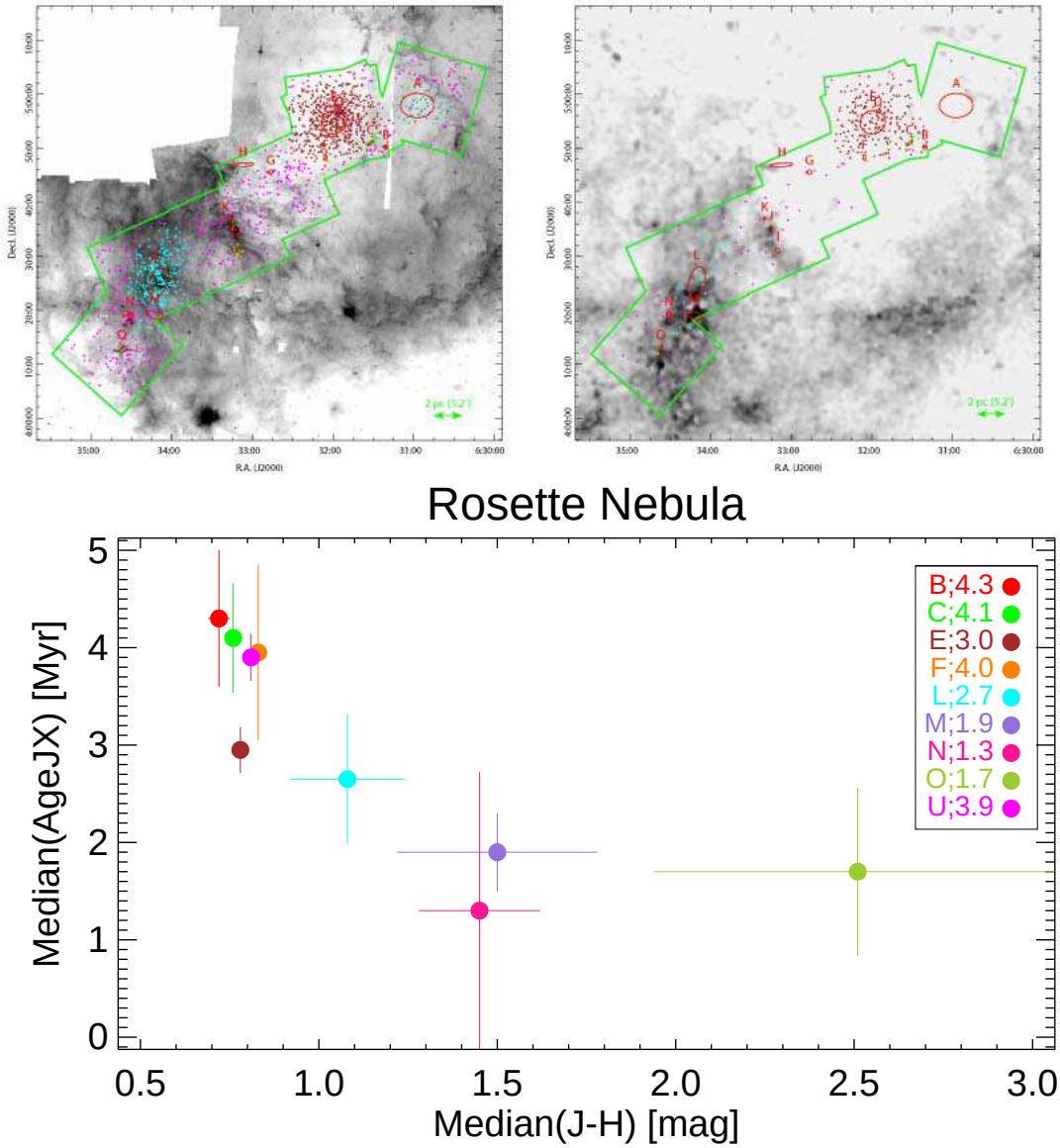

Fig. 12.— Age_{JX} analysis of the Rosette Nebula. See Figure 7 for description. *Upper right:* The subset of MPCM stars available for Age_{JX} analysis and the elliptical contours superposed on the A_V map from Broos et al. (2013).

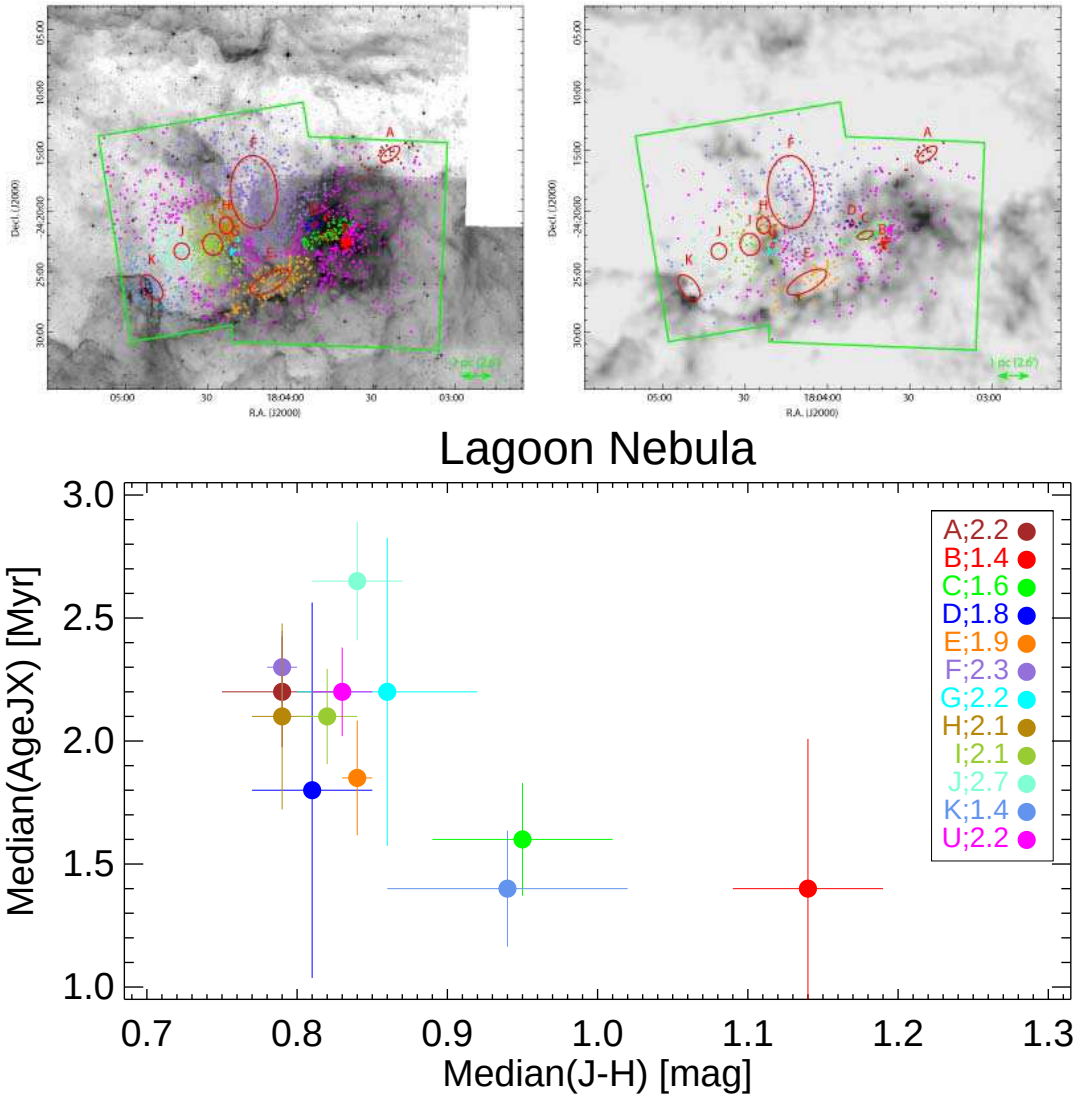

Fig. 13.— Age_{JX} analysis of the Lagoon Nebula. See Figure 7 for description. *Upper right:* The subset of MPCM stars available for Age_{JX} analysis and the elliptical contours superposed on the A_V map from Broos et al. (2013).

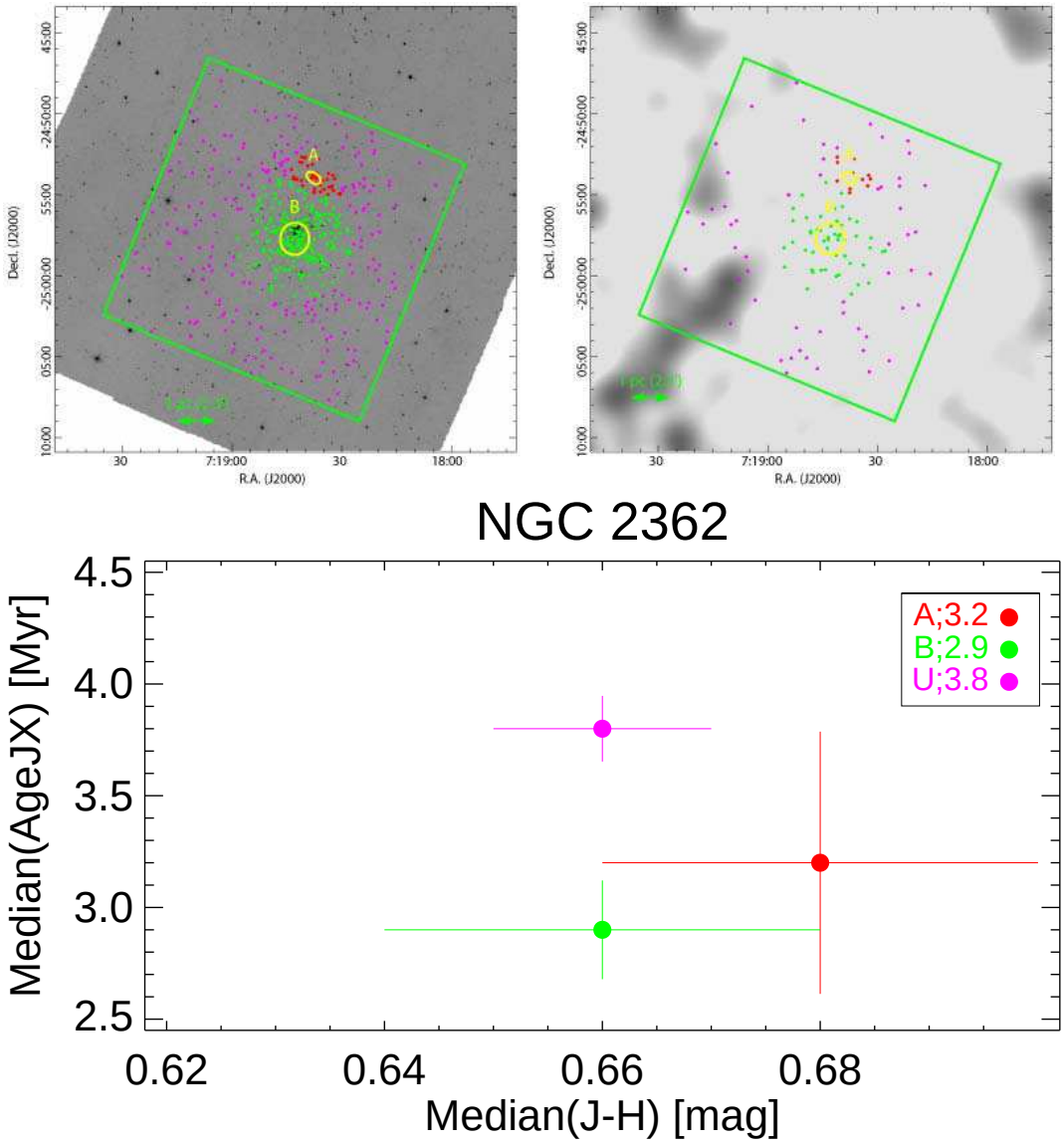

Fig. 14.— Age_{JX} analysis of NGC 2362. See Figure 7 for description. *Upper right:* The subset of MPCM stars available for Age_{JX} analysis and the elliptical contours superposed on the A_V map from Broos et al. (2013).

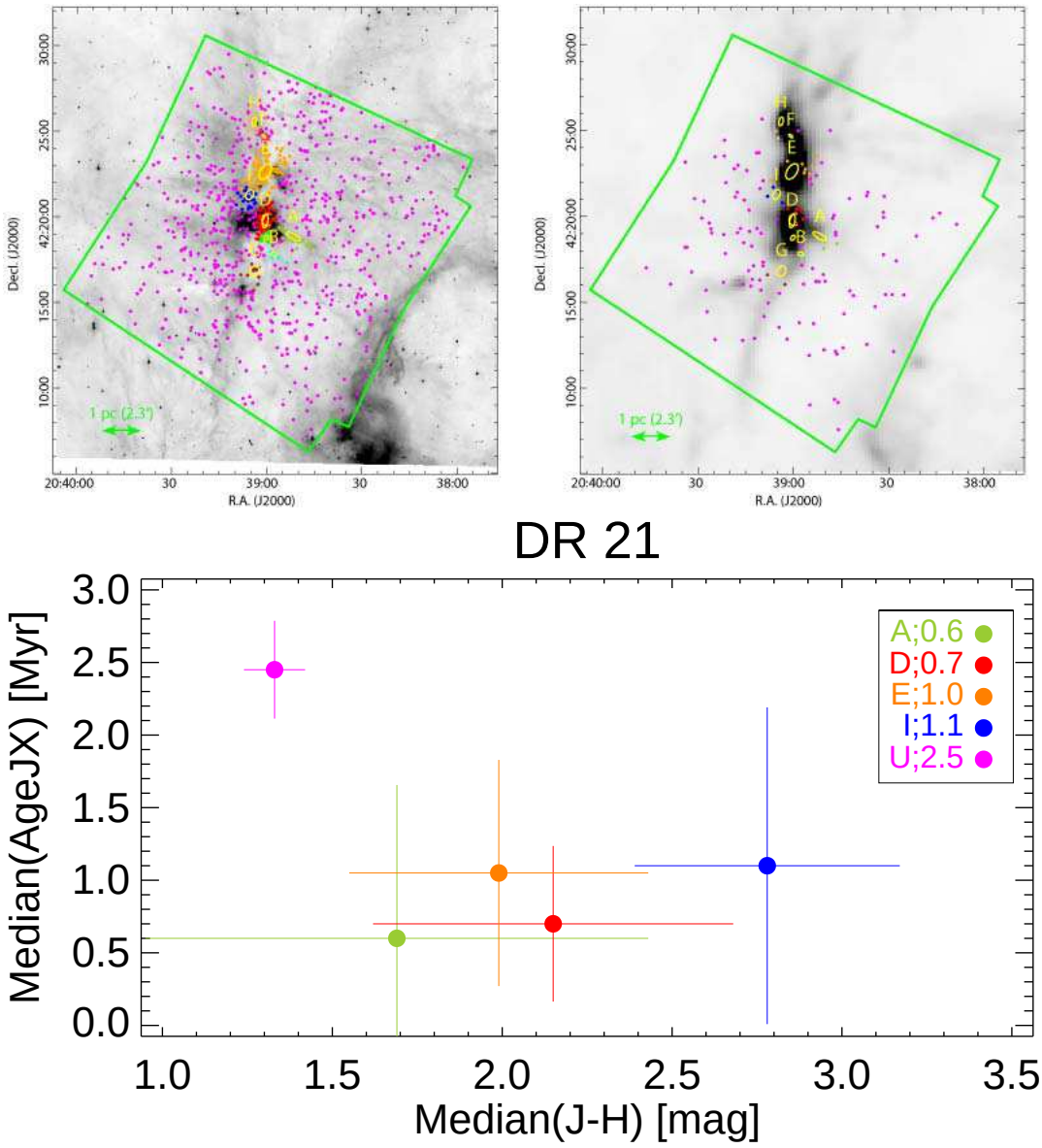

Fig. 15.— Age_{JX} analysis of DR 21. See Figure 7 for description.

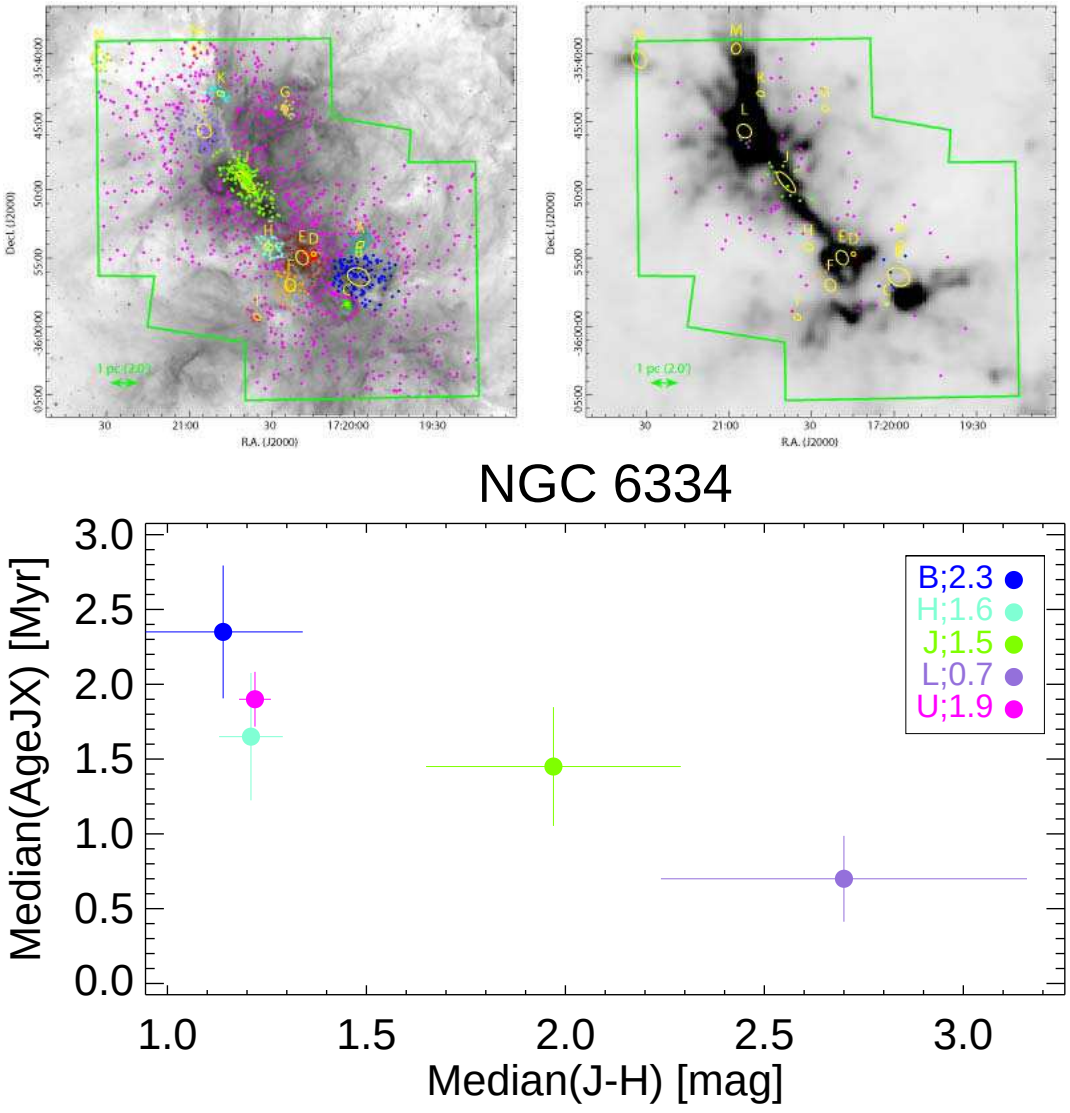

Fig. 16.— Age_{JX} analysis of NGC 6334. See Figure 7 for description.

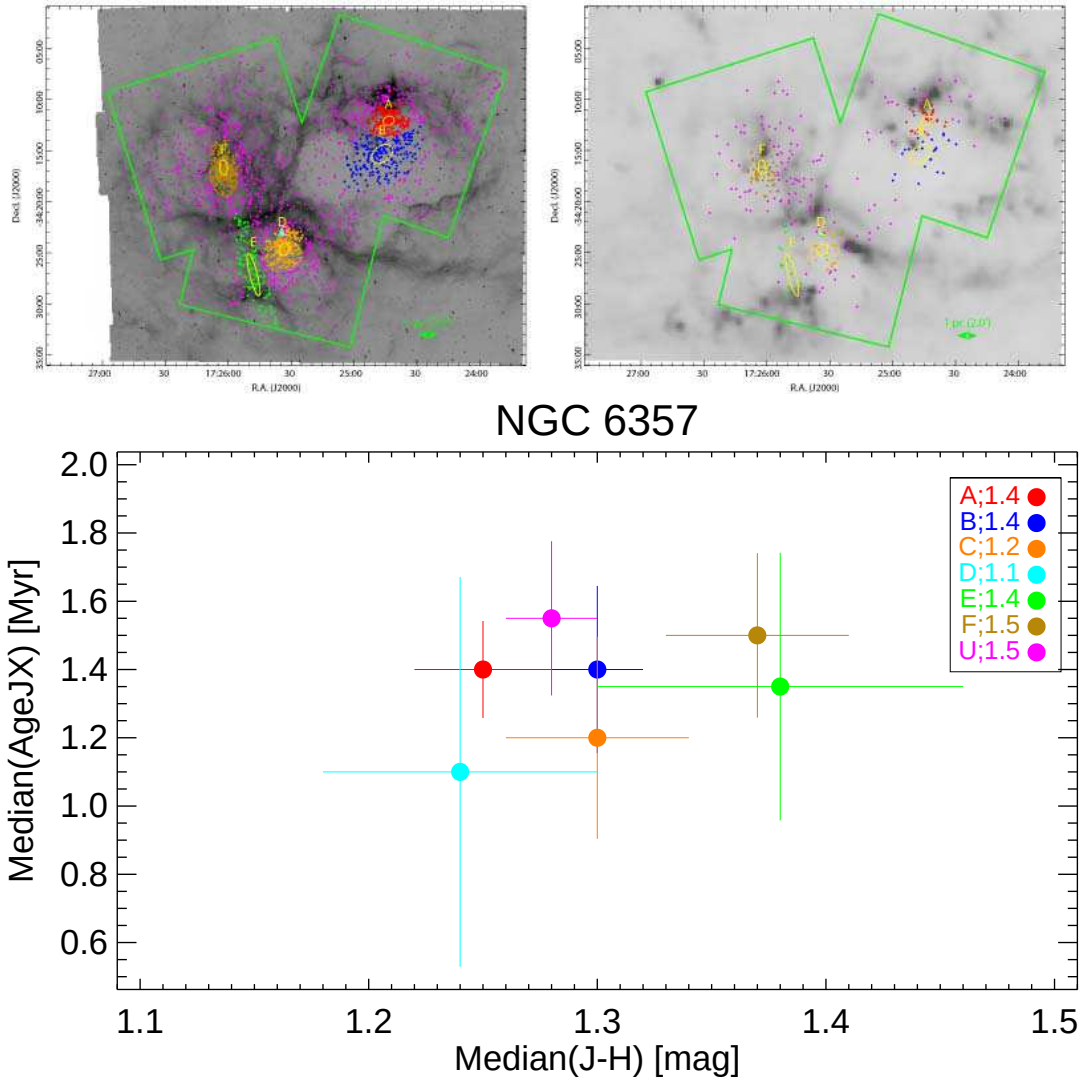

Fig. 17.— Age_{JX} analysis of NGC 6357. See Figure 7 for description.

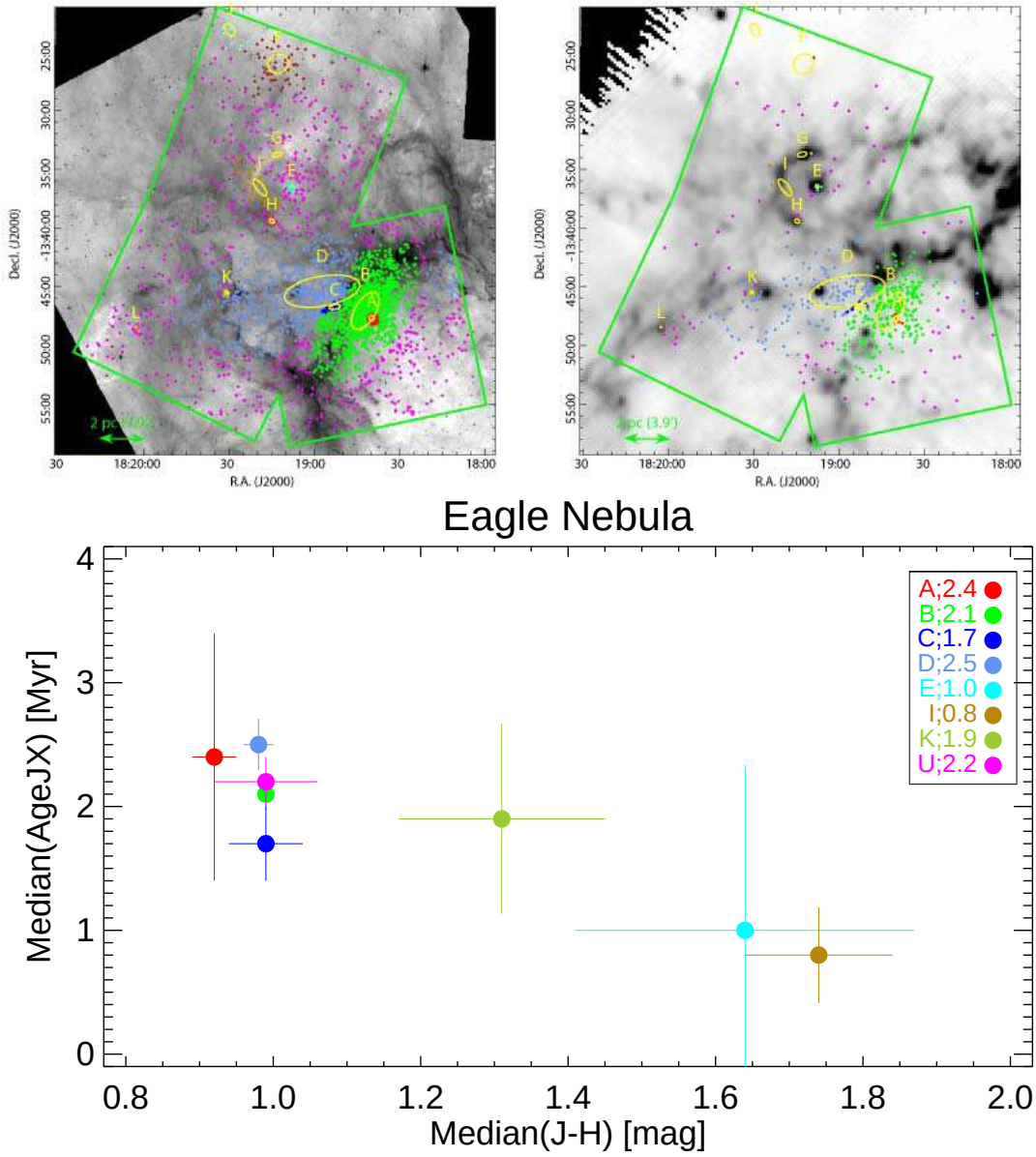

Fig. 18.— Age_{JX} analysis of the Eagle Nebula. See Figure 7 for description.

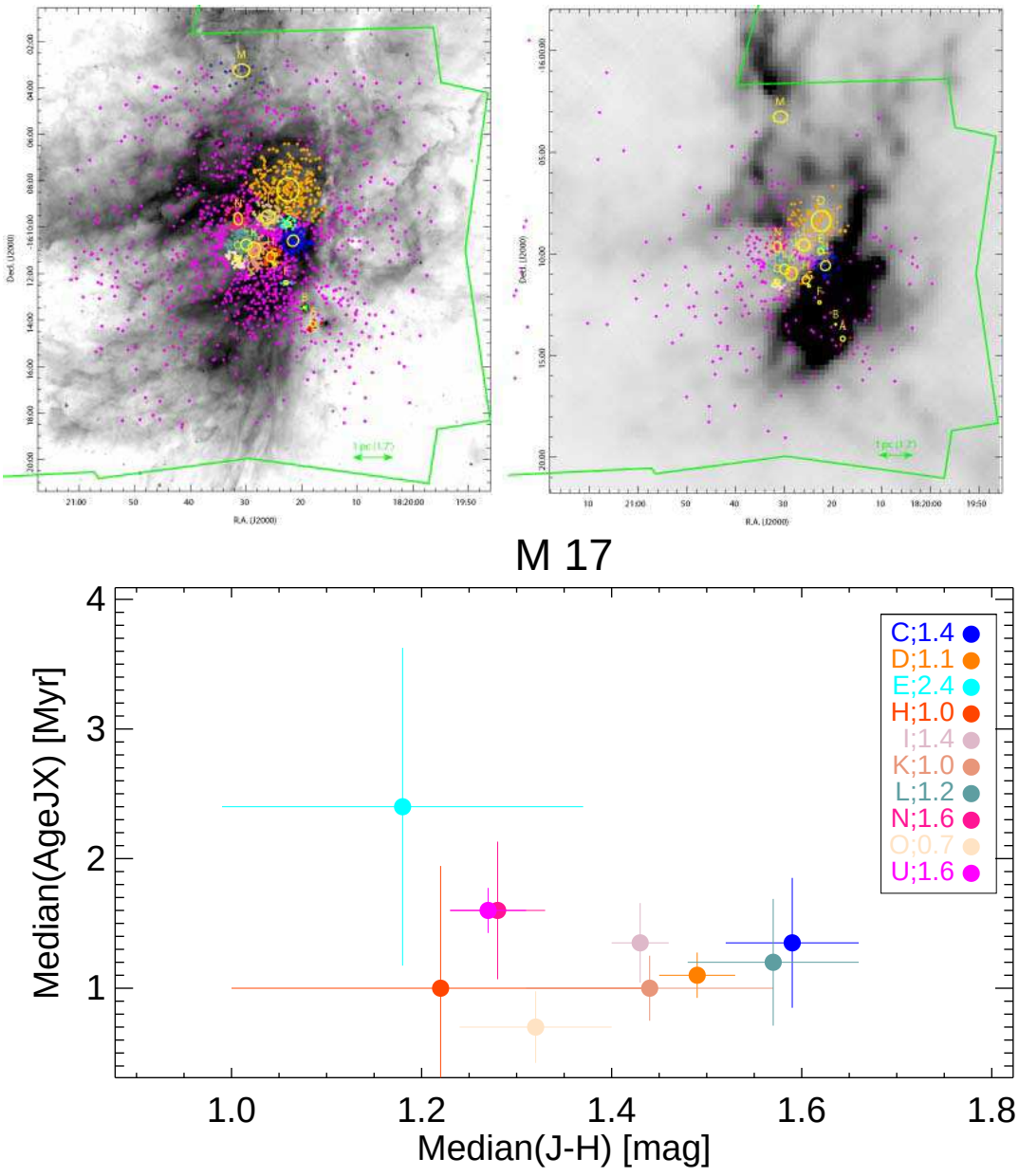

Fig. 19.— Age_{JX} analysis of M 17. See Figure 7 for description.

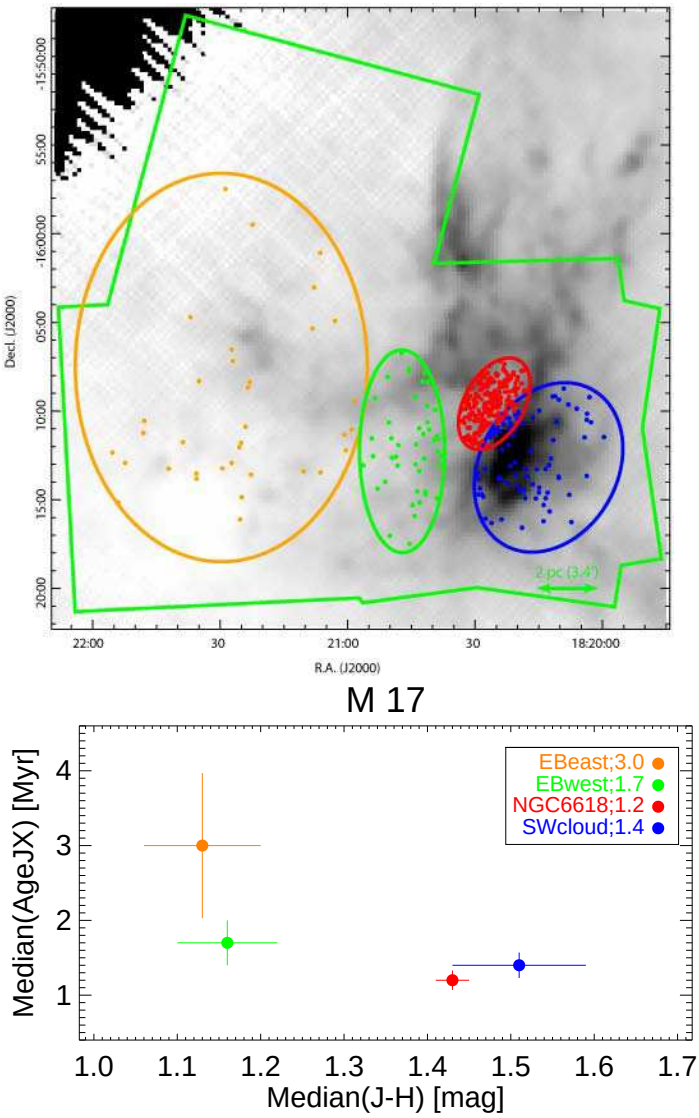

Fig. 20.— Special age analysis of M 17. *Upper:* The subset of MPCM stars available for Age_{JX} analysis stratified by the regions of special interest: the southwest molecular cloud (blue), the NGC 6618 cluster (red), the eastern (orange) and western (green) parts of Extended Bubble. The stars are superimposed on the 500 μm *Herschel*-SPIRE image. The *Chandra* field of view is outlined by the green polygon. *Lower:* The median Age_{JX} estimates for the four regions of interest plotted against their respective median $(J-H)$ color indices. The legend identifies each point with a region and states the median age in Myr.

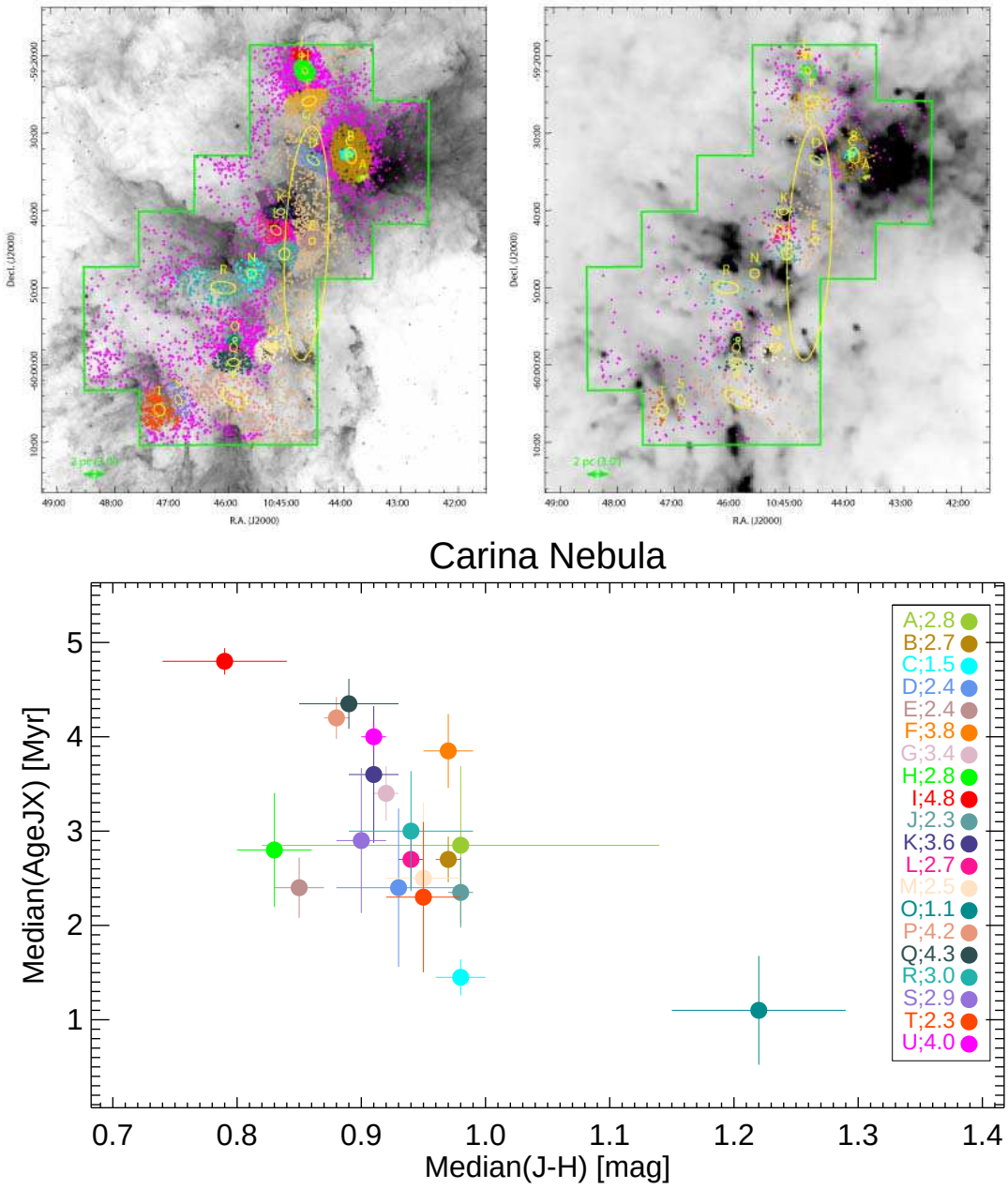

Fig. 21.— Age_{JX} analysis of the Carina Nebula complex. See Figure 7 for description.

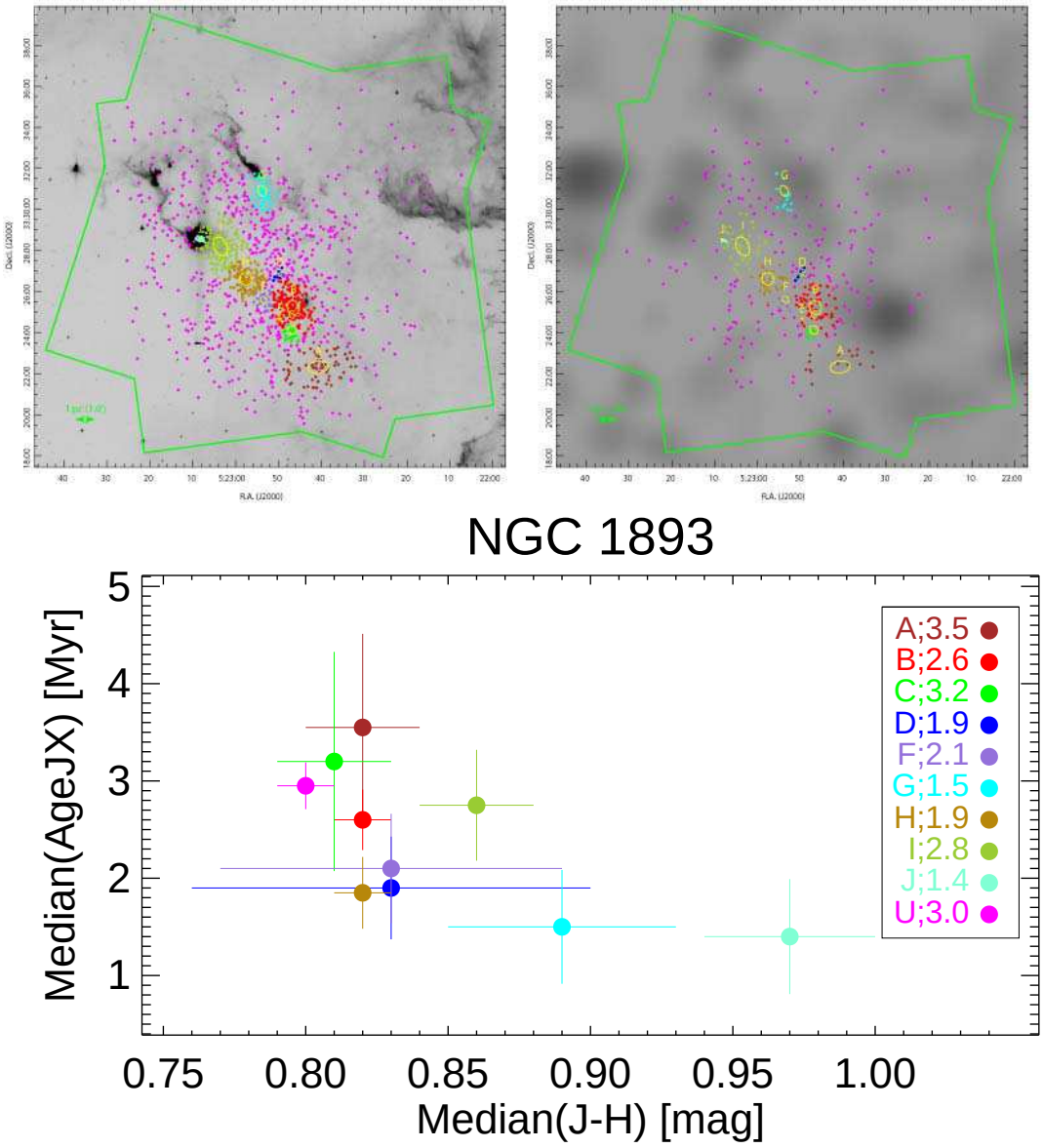

Fig. 22.— Age_{JX} analysis of NGC 1893. See Figure 7 for description. *Upper right:* The subset of MPCM stars available for Age_{JX} analysis and the elliptical contours superposed on the A_V map from Broos et al. (2013).

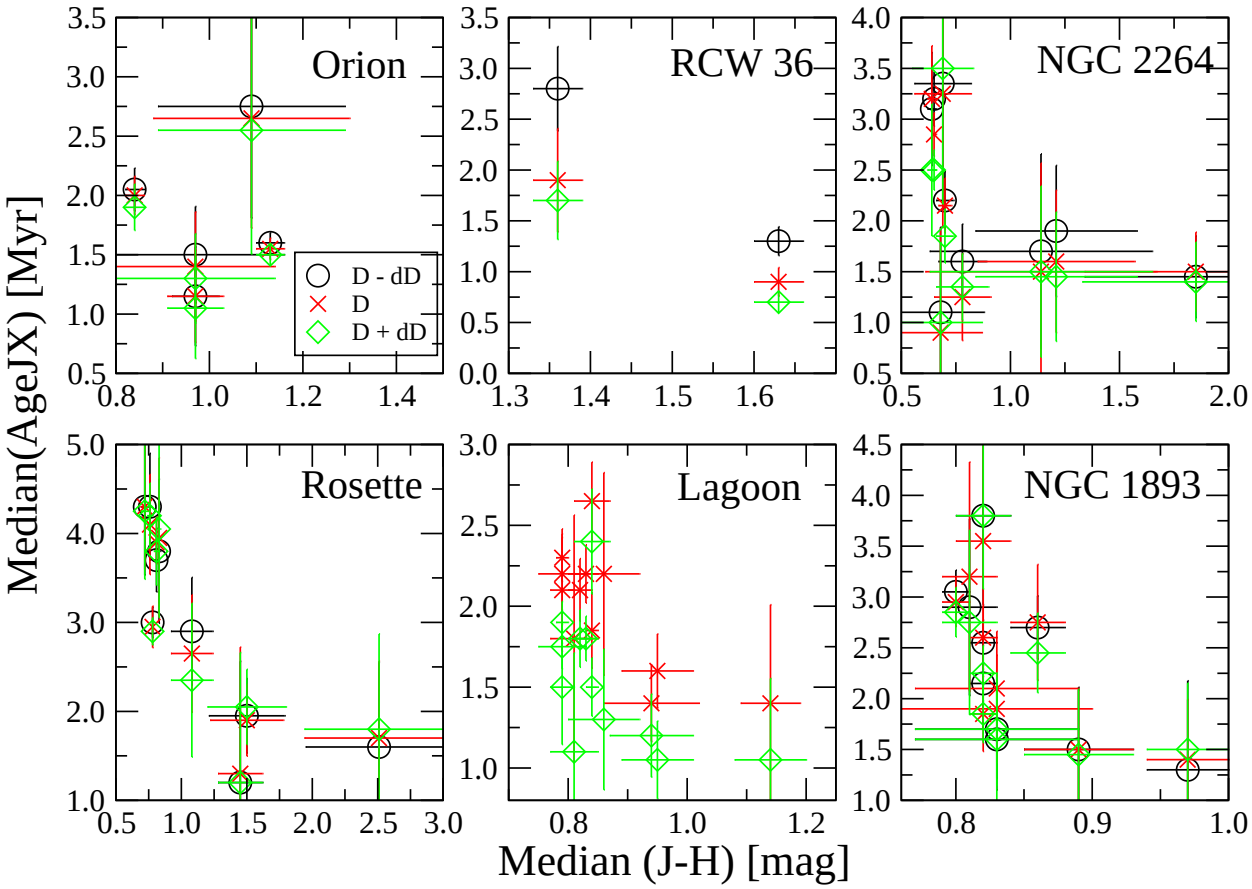

Fig. 23.— Effect of distance uncertainties on the resulted age gradients. The inferred median Age_{JX} for individual MYStIX subclusters plotted against their respective median $(J-H)$ color indices. The plots are given for the set of 6 exemplifying MYStIX regions (Orion, RCW 36, NGC 2264, Rosette, Lagoon, and NGC 1893) with distance errors reported in the literature (Feigelson et al. 2013, Table 1). The Age_{JX} vs. $J-H$ estimates are given for the set of tree trial distances to a MYStIX region: the reported mean/median distance measurement (red $\times$; same as in Figures 7 - 22), the reported lower boundary on distance (black $\circ$), and the reported upper boundary on distance (green $\diamond$).

Table 1. Individual Stellar Age Estimates

SF Region (1)	Source Name (2)	R.A. (J2000 deg) (3)	Decl. (J2000 deg) (4)	J (mag) (5)	H (mag) (6)	K_s (mag) (7)	L_X (10^{30} erg s^{-1}) (8)	A_J (mag) (9)	Age_{JX} (Myr) (10)	Mem (11)
NGC 1893	052242.31+332608.3	80.676310	33.435659	15.54 ± 0.01	14.75 ± 0.01	14.49 ± 0.01	2.11 ± 0.97	0.3	1.2	U
NGC 1893	052242.38+332422.0	80.676610	33.406116	17.15 ± 0.01	16.27 ± 0.01	15.96 ± 0.01	1.62 ± 0.78	0.5	4.6	B
NGC 1893	052242.55+333256.6	80.677320	33.549070	15.62 ± 0.01	14.94 ± 0.01	14.75 ± 0.01	0.41 ± 0.18	0.0	0.7	U
NGC 1893	052242.63+332449.4	80.677660	33.413723	15.88 ± 0.01	14.91 ± 0.01	14.51 ± 0.01	2.98 ± 1.95	0.8	1.0	B
NGC 1893	052242.67+332454.9	80.677820	33.415276	17.36 ± 0.01	16.40 ± 0.01	16.00 ± 0.01	1.66 ± 1.01	0.8	3.5	B
NGC 1893	052242.86+332445.6	80.678620	33.412678	16.50 ± 0.01	15.55 ± 0.01	15.15 ± 0.01	2.60 ± 1.25	0.8	2.6	B
NGC 1893	052243.04+332632.0	80.679364	33.442225	16.34 ± 0.01	15.57 ± 0.01	15.28 ± 0.01	3.05 ± 1.40	0.3	4.1	U
NGC 1893	052243.25+332011.0	80.680220	33.336400	16.03 ± 0.01	15.30 ± 0.01	14.95 ± 0.01	1.69 ± 1.12	0.3	1.9	U
NGC 1893	052243.25+332735.4	80.680249	33.459840	17.19 ± 0.01	16.35 ± 0.01	16.08 ± 0.01	1.50 ± 0.86	0.4	4.6	U
NGC 1893	052243.31+332641.1a	80.680470	33.444770	17.42 ± 0.01	16.58 ± 0.01	16.15 ± 0.02	0.34 ± 0.21	0.6	1.7	U

Note. — This table is available in its entirety (5525 MYStIX stars) in the machine-readable form in the on-line journal. A portion is shown here for guidance regarding its form and content. Column 1: Name of a star forming region. Column 2: MYStIX source's IAU designation. Columns 3 and 4: Right ascension and declination for epoch J2000.0 in degrees. Columns 5-7: NIR JHK_s magnitudes from Broos et al. (2013). Column 8: Intrinsic X-ray luminosity in the $(0.5 - 8)$ keV band from Broos et al. (2013). The statistical and systematic errors on L_X are summed in quadrature. Column

9: Estimate of the source extinction in the J-band. Column 10: Age_{JX} estimate. Individual age estimates of 5 Myr indicate that ages run into our truncation limit of 5 Myr. Column 11: Cluster membership from Kuhn et al. (2014). Unclustered or ambiguous stars are denoted as 'U'. All Age_{JX} members of the W 3, W 4, and NGC 3576 regions are denoted as 'U', since these regions were omitted from the analyses of Kuhn et al.

Table 2. Age Estimates for the MYStIX Clusters

SF Region	MYStIX Cluster	R.A. (J2000 deg)	Decl. (J2000 deg)	R' ($4R_c{}'$)	R_{pc} ($4R_c$ pc)	N_{tot}	$median$ $(J-H)_{tot}$ (mag)	N_{AgeJX}	$median$ $(J-H)_{AgeJX}$ (mag)	$median$ (Age_{JX}) (Myr)	$\mathrm{Age_{JH}}$ (Myr)
(1)	(2)	(3)	(4)	(5)	(6)	(7)	(8)	(9)	(10)	(11)	(12)
Orion	A	83.811003	-5.375278	0.4	0.0	25	1.0	9	1.0 ± 0.2	1.4 ± 0.5	···
Orion	B	83.815418	-5.389725	1.6	0.2	41	0.9	20	1.0 ± 0.1	1.1 ± 0.4	···
Orion	C	83.819538	-5.376180	7.7	0.9	1211	1.1	522	1.1 ± 0.0	1.5 ± 0.1	···
Orion	D	83.824266	-5.276333	4.4	0.5	30	1.2	12	1.1 ± 0.2	2.7 ± 0.9	···
Orion	U	···	···	···	···	217	0.8	94	0.8 ± 0.0	2.0 ± 0.2	···
Flame	A	85.427087	-1.903796	4.2	0.5	343	1.8	56	1.7 ± 0.1	0.8 ± 0.2	1.1:
Flame	U	···	···	···	···	141	1.3	47	1.3 ± 0.1	1.3 ± 0.3	···
W 40	A	277.861454	-2.094043	4.5	0.6	235	2.1	68	1.9 ± 0.1	0.8 ± 0.1	0.9:
W 40	U	···	···	···	···	191	1.9	34	1.6 ± 0.1	1.5 ± 0.2	1.0:
RCW 36	A	134.863096	-43.755983	3.2	0.6	227	1.7	40	1.6 ± 0.0	0.9 ± 0.1	1.1:
RCW 36	B	134.863598	-43.757322	0.4	0.1	32	2.2	···	···	···	0.9:
RCW 36	U	···	···	···	···	49	1.4	43	1.4 ± 0.0	1.9 ± 0.5	···
NGC 2264	A	100.131244	9.831153	1.3	0.3	17	0.9	5	0.7 ± 0.2	0.9 ± 1.0	···
NGC 2264	B	100.154592	9.791891	0.4	0.1	9	0.6	···	···	···	···
NGC 2264	C	100.168359	9.851570	0.4	0.1	6	···	···	···	···	···
NGC 2264	D	100.191014	9.817594	1.8	0.5	21	0.6	4	0.7 ± 0.1	3.2 ± 1.3	···

Table 2—Continued

SF	MYStIX	R.A.	Decl.	R'	R_{pc}	N_{tot}	$median$ $(J-H)_{tot}$	N_{AgeJX}	$median$ $(J-H)_{AgeJX}$	$median$ (Age_{JX})	$\mathrm{Age_{JH}}$
Region	Cluster	(J2000 deg)		$(4R_c{}')$	($4R_c$ pc)		(mag)		(mag)	(Myr)	(Myr)
(1)	(2)	(3)	(4)	(5)	(6)	(7)	(8)	(9)	(10)	(11)	(12)
NGC 2264	E	100.246348	9.872885	3.5	0.9	86	0.6	23	0.6 ± 0.0	3.2 ± 0.5	···
NGC 2264	F	100.246812	9.899766	0.8	0.2	19	0.6	···	···	···	···
NGC 2264	G	100.247385	9.603203	1.3	0.3	33	2.2	10	1.9 ± 0.5	1.5 ± 0.4	0.9:
NGC 2264	H	100.258800	9.812112	2.6	0.7	30	0.6	···	···	···	···
NGC 2264	I	100.268675	9.599235	1.2	0.3	55	1.1	9	1.1 ± 0.5	1.5 ± 1.1	···
NGC 2264	J	100.276199	9.569136	2.2	0.6	105	1.2	20	1.2 ± 0.4	1.6 ± 0.7	···
NGC 2264	K	100.284295	9.498011	2.7	0.7	104	0.7	34	0.7 ± 0.0	2.2 ± 0.3	···
NGC 2264	L	100.303280	9.486087	0.4	0.1	13	1.8	···	···	···	1.0:
NGC 2264	M	100.312268	9.444966	1.2	0.3	27	0.8	10	0.8 ± 0.1	1.2 ± 0.4	···
NGC 2264	U	···	···	···	···	648	0.6	176	0.6 ± 0.0	2.8 ± 0.2	···
Rosette	A	97.737964	4.965760	10.7	4.1	49	0.8	···	···	···	···
Rosette	B	97.835327	4.837189	1.6	0.6	8	0.7	4	0.7 ± 0.0	4.3 ± 0.7	···
Rosette	C	97.883154	4.849333	1.9	0.7	21	0.8	11	0.8 ± 0.0	4.1 ± 0.6	···
Rosette	D	97.980824	4.944177	0.9	0.4	22	0.6	···	···	···	···
Rosette	E	97.996974	4.913893	9.1	3.5	637	0.8	202	0.8 ± 0.0	3.0 ± 0.2	···
Rosette	F	98.022888	4.805445	1.5	0.6	9	0.8	4	0.8 ± 0.0	4.0 ± 0.9	···

Table 2—Continued

SF	MYStIX	R.A.	Decl.	R'	R_{pc}	N_{tot}	$median$ $(J-H)_{tot}$	N_{AgeJX}	$median$ $(J-H)_{AgeJX}$	$median$ (Age_{JX})	$\mathrm{Age_{JH}}$
Region	Cluster	(J2000 deg)		$(4R_c')$	$(4R_c$ pc)		(mag)		(mag)	(Myr)	(Myr)
(1)	(2)	(3)	(4)	(5)	(6)	(7)	(8)	(9)	(10)	(11)	(12)
Rosette	G	98.193852	4.759768	1.6	0.6	3	···	···	···	···	···
Rosette	H	98.279829	4.782528	4.8	1.9	44	0.8	···	···	···	···
Rosette	I	98.292418	4.517794	1.9	0.7	15	1.0	···	···	···	···
Rosette	J	98.312868	4.585495	1.3	0.5	11	2.2	···	···	···	0.9:
Rosette	K	98.333639	4.616929	0.9	0.4	5	···	···	···	···	···
Rosette	L	98.544391	4.418399	8.9	3.5	265	1.1	24	1.1 ± 0.2	2.7 ± 0.7	···
Rosette	M	98.553634	4.318479	4.6	1.8	75	2.2	4	1.5 ± 0.3	1.9 ± 0.4	0.9:
Rosette	N	98.630872	4.319126	1.8	0.7	36	1.6	9	1.5 ± 0.2	1.3 ± 1.4	1.2:
Rosette	O	98.654683	4.217308	1.4	0.6	20	1.8	3	2.5 ± 0.6	1.7 ± 0.9	1.1:
Rosette	U	···	···	···	···	510	0.8	65	0.8 ± 0.0	3.9 ± 0.2	···
Lagoon	A	270.849088	-24.255214	2.7	1.0	39	0.9	20	0.8 ± 0.0	2.2 ± 0.2	···
Lagoon	B	270.917151	-24.377850	0.6	0.2	74	1.2	20	1.1 ± 0.1	1.4 ± 0.6	···
Lagoon	C	270.943049	-24.367034	2.0	0.7	81	0.9	24	0.9 ± 0.1	1.6 ± 0.2	···
Lagoon	D	270.963550	-24.352091	0.8	0.3	23	0.8	9	0.8 ± 0.0	1.8 ± 0.8	···
Lagoon	E	271.031512	-24.431435	5.1	1.9	139	0.8	48	0.8 ± 0.0	1.9 ± 0.2	···
Lagoon	F	271.055521	-24.307465	9.9	3.7	500	0.8	191	0.8 ± 0.0	2.3 ± 0.1	···

Table 2—Continued

SF	MYStIX	R.A.	Decl.	R'	R_{pc}	N_{tot}	$median$ $(J-H)_{tot}$	N_{AgeJX}	$median$ $(J-H)_{AgeJX}$	$median$ (Age_{JX})	$\mathrm{Age_{JH}}$
Region	Cluster	(J2000 deg)		$(4R_c{}')$	$(4R_c$ pc)		(mag)		(mag)	(Myr)	(Myr)
(1)	(2)	(3)	(4)	(5)	(6)	(7)	(8)	(9)	(10)	(11)	(12)
Lagoon	G	271.083619	-24.380807	0.7	0.3	33	0.8	11	0.9 ± 0.1	2.2 ± 0.6	···
Lagoon	H	271.097216	-24.353499	2.5	0.9	143	0.8	37	0.8 ± 0.0	2.1 ± 0.4	···
Lagoon	I	271.117721	-24.379582	3.5	1.3	229	0.8	64	0.8 ± 0.0	2.1 ± 0.2	···
Lagoon	J	271.164951	-24.388953	2.6	1.0	76	0.9	22	0.8 ± 0.0	2.7 ± 0.2	···
Lagoon	K	271.210306	-24.438561	3.8	1.4	127	1.0	19	0.9 ± 0.1	1.4 ± 0.2	···
Lagoon	U	···	···	···	···	592	0.8	171	0.8 ± 0.0	2.2 ± 0.2	···
NGC 2362	A	109.657400	-24.899454	1.6	0.7	44	0.6	11	0.7 ± 0.0	3.2 ± 0.6	···
NGC 2362	B	109.678847	-24.962153	3.8	1.6	240	0.6	51	0.7 ± 0.0	2.9 ± 0.2	···
NGC 2362	U	···	···	···	···	207	0.6	57	0.7 ± 0.0	3.8 ± 0.1	···
DR 21	A	309.715318	42.314510	1.2	0.5	19	2.1	3	1.7 ± 0.7	0.6 ± 1.1	0.9:
DR 21	B	309.740409	42.297373	0.5	0.2	9	2.0	···	···	···	1.0:
DR 21	C	309.750805	42.313176	0.5	0.2	22	3.0	···	···	···	0.6:
DR 21	D	309.751734	42.329353	1.1	0.5	96	2.9	7	2.2 ± 0.5	0.7 ± 0.5	0.6:
DR 21	E	309.752011	42.377500	1.6	0.7	109	2.5	8	2.0 ± 0.4	1.0 ± 0.8	0.8:
DR 21	F	309.753634	42.411888	0.4	0.2	15	···	···	···	···	···
DR 21	G	309.765774	42.280760	1.1	0.5	13	2.7	···	···	···	0.7:

Table 2—Continued

SF	MYStIX	R.A.	Decl.	R'	R_{pc}	N_{tot}	$median$ $(J-H)_{tot}$	N_{AgeJX}	$median$ $(J-H)_{AgeJX}$	$median$ (Age_{JX})	$\mathrm{Age_{JH}}$
Region	Cluster	(J2000 deg)		$(4R_c{}')$	$(4R_c$ pc)		(mag)		(mag)	(Myr)	(Myr)
(1)	(2)	(3)	(4)	(5)	(6)	(7)	(8)	(9)	(10)	(11)	(12)
DR 21	H	309.766340	42.426072	0.8	0.3	31	3.0	···	···	···	0.6:
DR 21	I	309.772383	42.354995	1.0	0.4	24	3.0	4	2.8 ± 0.4	1.1 ± 1.1	0.6:
DR 21	U	···	···	···	···	641	1.6	110	1.3 ± 0.1	2.5 ± 0.3	1.3:
NGC 6334	A	259.991145	-35.900501	1.0	0.5	38	1.4	···	···	···	···
NGC 6334	B	259.993594	-35.939946	3.0	1.5	129	1.4	6	1.1 ± 0.2	2.3 ± 0.4	···
NGC 6334	C	260.011243	-35.973044	0.5	0.2	17	1.1	···	···	···	···
NGC 6334	D	260.061955	-35.912041	0.6	0.3	18	1.9	···	···	···	1.0:
NGC 6334	E	260.079016	-35.916462	1.9	1.0	100	1.9	···	···	···	1.0:
NGC 6334	F	260.096742	-35.950008	1.7	0.8	39	1.3	···	···	···	···
NGC 6334	G	260.104977	-35.734512	0.9	0.4	25	1.6	···	···	···	1.2:
NGC 6334	H	260.130189	-35.903772	1.2	0.6	40	1.4	4	1.2 ± 0.1	1.6 ± 0.4	···
NGC 6334	I	260.146879	-35.988912	0.9	0.5	12	1.0	···	···	···	···
NGC 6334	J	260.163313	-35.824230	2.6	1.3	225	2.2	14	2.0 ± 0.3	1.5 ± 0.4	0.9:
NGC 6334	K	260.201620	-35.716380	0.9	0.5	19	3.0	···	···	···	0.6:
NGC 6334	L	260.226540	-35.761934	2.0	1.0	122	2.7	5	2.7 ± 0.5	0.7 ± 0.3	0.7:
NGC 6334	M	260.238922	-35.661256	1.4	0.7	19	···	···	···	···	···

Table 2—Continued

SF	MYStIX	R.A.	Decl.	R'	R_{pc}	N_{tot}	$median$ $(J-H)_{tot}$	N_{AgeJX}	$median$ $(J-H)_{AgeJX}$	$median$ (Age_{JX})	$\mathrm{Age_{JH}}$
Region	Cluster	(J2000 deg)		$(4R_c{}')$	$(4R_c$ pc)		(mag)		(mag)	(Myr)	(Myr)
(1)	(2)	(3)	(4)	(5)	(6)	(7)	(8)	(9)	(10)	(11)	(12)
NGC 6334	N	260.385219	-35.674128	2.3	1.1	15	2.2	···	···	···	0.9:
NGC 6334	U	···	···	···	···	845	1.4	75	1.2 ± 0.0	1.9 ± 0.2	···
NGC 6357	A	261.181999	-34.201943	2.0	1.0	282	1.3	29	1.2 ± 0.0	1.4 ± 0.1	···
NGC 6357	B	261.194671	-34.256275	3.9	1.9	239	1.3	23	1.3 ± 0.0	1.4 ± 0.2	···
NGC 6357	C	261.388830	-34.412054	2.2	1.1	229	1.3	27	1.3 ± 0.0	1.2 ± 0.3	···
NGC 6357	D	261.392877	-34.385974	0.4	0.2	49	1.3	8	1.2 ± 0.1	1.1 ± 0.6	···
NGC 6357	E	261.449624	-34.453379	5.0	2.5	126	1.3	14	1.4 ± 0.1	1.4 ± 0.4	···
NGC 6357	F	261.508987	-34.278275	2.2	1.1	299	1.4	59	1.4 ± 0.0	1.5 ± 0.2	···
NGC 6357	U	···	···	···	···	1011	1.4	138	1.3 ± 0.0	1.5 ± 0.2	···
Eagle	A	274.666334	-13.794696	0.9	0.5	56	0.9	6	0.9 ± 0.0	2.4 ± 1.0	···
Eagle	B	274.675703	-13.784286	5.3	2.7	1117	1.0	253	1.0 ± 0.0	2.1 ± 0.1	···
Eagle	C	274.720055	-13.778617	1.4	0.7	39	1.0	10	1.0 ± 0.1	1.7 ± 0.3	···
Eagle	D	274.738796	-13.756268	9.0	4.6	542	1.0	127	1.0 ± 0.0	2.5 ± 0.2	···
Eagle	E	274.782841	-13.607665	0.6	0.3	23	2.4	3	1.6 ± 0.2	1.0 ± 1.3	0.8:
Eagle	F	274.803157	-13.434045	3.3	1.7	55	1.6	···	···	···	1.2:
Eagle	G	274.804783	-13.562508	1.2	0.6	25	2.6	···	···	···	0.7:

Table 2—Continued

SF	MYStIX	R.A.	Decl.	R'	R_{pc}	N_{tot}	$median$ $(J-H)_{tot}$	N_{AgeJX}	$median$ $(J-H)_{AgeJX}$	$median$ (Age_{JX})	$\mathrm{Age_{JH}}$
Region	Cluster	(J2000 deg)		$(4R_c{}')$	$(4R_c$ pc)		(mag)		(mag)	(Myr)	(Myr)
(1)	(2)	(3)	(4)	(5)	(6)	(7)	(8)	(9)	(10)	(11)	(12)
Eagle	H	274.812350	-13.656935	0.8	0.4	13	1.6	···	···	···	1.3:
Eagle	I	274.829961	-13.609316	2.3	1.2	44	1.7	5	1.7 ± 0.1	0.8 ± 0.4	1.2:
Eagle	J	274.873687	-13.385557	1.9	1.0	15	1.5	···	···	···	1.4:
Eagle	K	274.877955	-13.758213	0.5	0.2	14	1.4	5	1.3 ± 0.1	1.9 ± 0.8	···
Eagle	L	275.011498	-13.807294	0.2	0.1	5	2.0	···	···	···	1.0:
Eagle	U	···	···	···	···	626	1.0	80	1.0 ± 0.1	2.2 ± 0.2	···
M 17	A	275.075084	-16.236297	0.5	0.3	13	2.0	···	···	···	1.0:
M 17	B	275.081195	-16.224450	0.2	0.1	7	2.5	···	···	···	0.8:
M 17	C	275.089865	-16.176439	0.9	0.6	77	1.7	18	1.6 ± 0.1	1.4 ± 0.5	1.1:
M 17	D	275.093603	-16.139853	1.9	1.1	257	1.5	75	1.5 ± 0.0	1.1 ± 0.2	1.4:
M 17	E	275.093839	-16.164482	0.6	0.3	27	1.5	5	1.2 ± 0.2	2.4 ± 1.2	1.4:
M 17	F	275.095044	-16.206489	0.3	0.2	15	1.8	···	···	···	1.0:
M 17	G	275.104021	-16.192919	0.3	0.1	17	1.6	···	···	···	1.3:
M 17	H	275.106514	-16.188004	0.8	0.4	55	1.3	9	1.2 ± 0.2	1.0 ± 0.9	···
M 17	I	275.108478	-16.159423	1.2	0.7	83	1.4	40	1.4 ± 0.0	1.4 ± 0.3	···
M 17	J	275.115791	-16.165053	0.1	0.0	2	···	···	···	···	···

Table 2—Continued

SF	MYStIX	R.A.	Decl.	R'	R_{pc}	N_{tot}	$median$ $(J-H)_{tot}$	N_{AgeJX}	$median$ $(J-H)_{AgeJX}$	$median$ (Age_{JX})	$\mathrm{Age_{JH}}$
Region	Cluster	(J2000 deg)		$(4R_c{}')$	$(4R_c$ pc)		(mag)		(mag)	(Myr)	(Myr)
(1)	(2)	(3)	(4)	(5)	(6)	(7)	(8)	(9)	(10)	(11)	(12)
M 17	K	275.118917	-16.182870	1.2	0.7	98	1.4	19	1.4 ± 0.1	1.0 ± 0.3	···
M 17	L	275.124664	-16.179366	0.9	0.5	142	1.8	30	1.6 ± 0.1	1.2 ± 0.5	1.0:
M 17	M	275.128330	-16.054331	1.2	0.7	27	1.8	···	···	···	1.0:
M 17	N	275.130814	-16.160819	0.9	0.5	71	1.3	23	1.3 ± 0.1	1.6 ± 0.5	···
M 17	O	275.131351	-16.189476	0.5	0.3	48	1.4	11	1.3 ± 0.1	0.7 ± 0.3	···
M 17	U	···	···	···	···	1031	1.4	263	1.3 ± 0.0	1.6 ± 0.2	···
Carina	A	160.924382	-59.596843	0.8	0.6	42	1.0	6	1.0 ± 0.2	2.8 ± 0.8	···
Carina	B	160.975828	-59.550664	3.4	2.3	962	1.0	111	1.0 ± 0.0	2.7 ± 0.2	···
Carina	C	160.985040	-59.548341	1.2	0.8	294	0.9	30	1.0 ± 0.0	1.5 ± 0.2	···
Carina	D	161.137282	-59.561635	2.7	1.8	119	0.9	15	0.9 ± 0.1	2.4 ± 0.8	···
Carina	E	161.141734	-59.735484	1.7	1.1	129	0.8	28	0.9 ± 0.0	2.4 ± 0.3	···
Carina	F	161.155625	-59.434109	3.1	2.1	169	0.9	42	1.0 ± 0.0	3.8 ± 0.4	···
Carina	G	161.165355	-59.740477	36.0	24.1	1122	0.9	202	0.9 ± 0.0	3.4 ± 0.3	···
Carina	H	161.174039	-59.367985	1.6	1.0	242	0.8	24	0.8 ± 0.0	2.8 ± 0.6	···
Carina	I	161.188758	-59.335179	1.2	0.8	91	0.8	8	0.8 ± 0.1	4.8 ± 0.1	···
Carina	J	161.260036	-59.763797	2.9	1.9	231	1.0	48	1.0 ± 0.0	2.3 ± 0.4	···

Table 2—Continued

SF	MYStIX	R.A.	Decl.	R'	R_{pc}	N_{tot}	$median$ $(J-H)_{tot}$	N_{AgeJX}	$median$ $(J-H)_{AgeJX}$	$median$ (Age_{JX})	$\mathrm{Age_{JH}}$
Region	Cluster	(J2000 deg)		$(4R_c{}')$	$(4R_c$ pc)		(mag)		(mag)	(Myr)	(Myr)
(1)	(2)	(3)	(4)	(5)	(6)	(7)	(8)	(9)	(10)	(11)	(12)
Carina	K	161.275744	-59.672471	1.8	1.2	86	0.9	19	0.9 ± 0.0	3.6 ± 0.7	···
Carina	L	161.296066	-59.712681	2.5	1.7	230	0.9	58	0.9 ± 0.0	2.7 ± 0.3	···
Carina	M	161.307215	-59.966023	2.4	1.6	169	0.9	34	0.9 ± 0.0	2.5 ± 0.8	···
Carina	N	161.400506	-59.805549	2.3	1.5	85	1.4	···	···	···	···
Carina	O	161.472697	-59.948001	1.1	0.7	73	1.1	7	1.2 ± 0.1	1.1 ± 0.6	···
Carina	P	161.476497	-60.075608	5.3	3.5	305	0.9	74	0.9 ± 0.0	4.2 ± 0.2	···
Carina	Q	161.479838	-59.997525	2.5	1.7	155	0.9	20	0.9 ± 0.0	4.3 ± 0.3	···
Carina	R	161.522459	-59.835953	4.7	3.1	136	1.0	21	0.9 ± 0.1	3.0 ± 0.6	···
Carina	S	161.719518	-60.077775	2.1	1.4	108	0.9	13	0.9 ± 0.0	2.9 ± 0.8	···
Carina	T	161.801941	-60.099413	3.0	2.0	233	0.9	25	0.9 ± 0.0	2.3 ± 0.8	···
Carina	U	···	···	···	···	2353	0.9	354	0.9 ± 0.0	4.0 ± 0.2	···
NGC 1893	A	80.669746	33.372321	1.6	1.6	68	0.8	16	0.8 ± 0.0	3.5 ± 1.0	···
NGC 1893	B	80.693946	33.420652	1.3	1.3	180	0.8	54	0.8 ± 0.0	2.6 ± 0.3	···
NGC 1893	C	80.695468	33.402485	0.8	0.8	23	0.8	8	0.8 ± 0.0	3.2 ± 1.1	···
NGC 1893	D	80.706555	33.447851	0.4	0.4	14	0.8	7	0.8 ± 0.1	1.9 ± 0.5	···
NGC 1893	E	80.706743	33.411659	0.1	0.1	5	0.8	···	···	···	···

Table 2—Continued

SF	MYStIX	R.A.	Decl.	R'	R_{pc}	N_{tot}	$median$ $(J-H)_{tot}$	N_{AgeJX}	$median$ $(J-H)_{AgeJX}$	$median$ (Age_{JX})	$\mathrm{Age_{JH}}$
Region	Cluster	(J2000 deg)		$(4R_c{}')$	($4R_c$ pc)		(mag)		(mag)	(Myr)	(Myr)
(1)	(2)	(3)	(4)	(5)	(6)	(7)	(8)	(9)	(10)	(11)	(12)
NGC 1893	F	80.722654	33.426924	0.6	0.6	30	0.8	7	0.8 ± 0.1	2.1 ± 0.6	···
NGC 1893	G	80.724232	33.515267	0.9	1.0	55	0.9	14	0.9 ± 0.0	1.5 ± 0.6	···
NGC 1893	H	80.740159	33.443803	1.2	1.2	111	0.8	32	0.8 ± 0.0	1.9 ± 0.4	···
NGC 1893	I	80.764739	33.470349	1.6	1.7	148	0.8	46	0.9 ± 0.0	2.8 ± 0.6	···
NGC 1893	J	80.784690	33.476036	0.2	0.2	17	1.0	3	1.0 ± 0.0	1.4 ± 0.6	···
NGC 1893	U	···	···	···	···	624	0.8	166	0.8 ± 0.0	3.0 ± 0.2	···

Note. — Column 1: Name of a star forming region. Column 2: MYStIX cluster designation. Columns 3 and 4: Coordinates of the center of a MYStIX cluster. Right ascension and declination for epoch J2000.0 in degrees. Columns 5-6: Spatial extent of a MYStIX cluster; this is 4× cluster core radius in arc-minutes and parsecs, respectively. Columns 7-8: Total number of MYStIX stars assigned as cluster members and the median of their $J-H$ color (Kuhn et al. 2014). Columns 9-10: Number of Age_{JX} stars assigned as cluster members and the median of their $J-H$ color. Column 11: Cluster $median(Age_{JX})$ estimate. Column 12: For the heavily reddened MYStIX clusters, with $(J-H)_{tot} > 1.5$ mag, independent age estimates are given based on the calibration curve of Figure 4. The ':' indicates that these estimates could be quite uncertain.